

AD-A123 952




THE AERODYNAMIC PERFORMANCE OF SEVERAL FLOW CONTROL
DEVICES FOR INTERNAL... (U) NATIONAL AERONAUTICS AND
SPACE ADMINISTRATION WASHINGTON DC W T ECKERT ET AL.
DEC 82 NASA-A-8816 NASA-TP-1972

1/1

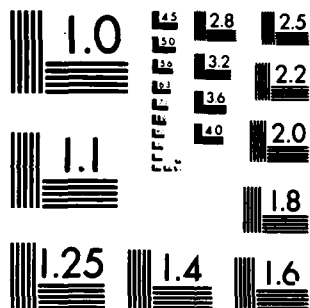
UNCLASSIFIED

F/G 20/4

NL

END
DATE
FILMED
83
DTIC



MICROCOPY RESOLUTION TEST CHART
NATIONAL BUREAU OF STANDARDS 1963 A



**NASA
Technical
Paper
1972**

**AVRADCOM
Technical
Report
82-A-2**

1982

The Aerodynamic Performance of Several Flow Control Devices for Internal Flow Systems

William T. Eckert
*Aeromechanics Laboratory
AVRADCOM Research and Technology Laboratories
Ames Research Center
Moffett Field, California*

Brian M. Wettlaufer
*Sverdrup Technology, Ames Division
Moffett Field, California*

Kenneth W. Mort
*Ames Research Center
Moffett Field, California*

NASA
National Aeronautics
and Space Administration

Scientific and Technical
Information Branch

A



SYMBOLS

A	local area, m^2 (ft^2)	δ	uncertainty in indicated value of parameter
C_p	static pressure coefficient, $(p_{si} - p_{s_{ref}})/q_1$	η	fan aerodynamic efficiency, percent
c	chord length measured along centerline of vane structure, cm (in.)	θ	deflection angle of turning vane panel, deg
c_v	vane chord length measured between leading and trailing edges, cm (in.)	ρ	static density of local flow, kg/m^3 ($slugs/ft^3$)
g	gap between straighteners, louver, or vane panels measured center-to-center along line of leading edges, cm (in.)	ϕ	overturn angle of flow exiting vane cascade, taken approximately one c_v length downstream of exit plane, deg
l/D	longitudinal position in test duct, fraction of hydraulic diameter	Subscripts:	
P	power required to overcome losses in wind tunnel or duct system, W (hp)	B	condition due to blockage
p	pressure, N/m^2 (lb/ft^2)	d	condition at wind tunnel or duct drive system
q	dynamic pressure, N/m^2 (lb/ft^2)	f	fillet
R_n	Reynolds number based on c_v	h	hinge location
r	radius, cm (in.)	i	condition at local measurement station
V	local flow velocity, m/sec (ft/sec)	net	net value
x	chordwise distance from nose of vane, measured along c , cm (in.)	ref	reference
y	vane thickness ordinate, measured perpendicular to c , cm (in.)	s	static condition
z	vane shape ordinate, measured perpendicular to c , cm (in.)	T	total or stagnation condition
β	geometric turning angle of vane cascade set, deg	t	tail
Δ	change in condition from upstream to downstream locations	tot	total
$\Delta p_T/q_1$	total pressure loss coefficient based on upstream dynamic pressure	o	condition at duct system reference station or test section
		1	flow condition upstream of component
		2	flow condition downstream of component

THE AERODYNAMIC PERFORMANCE OF SEVERAL FLOW CONTROL DEVICES FOR INTERNAL FLOW SYSTEMS

William T. Eckert,* Brian M. Wettlaufer,† and Kenneth W. Mort

Ames Research Center

An experimental research and development program was undertaken to develop and document new flow-control devices for use in the major modifications to the 40- by 80-Foot Wind Tunnel at Ames Research Center. These devices, which are applicable to other facilities as well, included grid-type and quasi-two-dimensional flow straighteners, louver panels for valving, and turning-vane cascades with net turning angles from 0° to 90°. The tests were conducted at model scale over a Reynolds number range from 2×10^5 to 17×10^5 , based on chord. The results showed quantitatively the performance benefits of faired, low-blockage, smooth-surface straightener systems, and the advantages of curved turning-vanes with hinge-line gaps sealed and a preferred chord-to-gap ratio between 2.5 and 3.0 for 45° or 90° turns.

BACKGROUND AND INTRODUCTION

Many internal flow systems, including most wind tunnels, employ turning-vane, louver, or flow-straightening cascade systems for flow control. These flow-control devices are used because of their beneficial effect on system aerodynamic performance. "System aerodynamic performance" includes (1) the related factors of power, energy, and pressure losses and (2) the secondary effects of the devices on the quality of the flow in downstream components. "Flow quality" includes flow uniformity, distributions, angularities, and turbulence. Many such flow-control devices have been studied and documented. For example, Idel'chik (1966) provides a major compilation of component losses that is a significant contribution to the literature.

But the number of possible variations in configuration, and thus performance, is nearly infinite. The recent NASA efforts to modify the 40- by 80-Foot Wind Tunnel at Ames Research Center (Mort et al., 1976, 1979) revealed the pressing need for additional vane, louver, and straightener performance data for configurations unique to the modification and thus not found in the literature. This report presents the results of an experimental program undertaken to fulfill the need for these new performance data.

The primary purpose of these experimental studies was to determine component pressure losses. However, for some configurations, exit flow angles or chordwise loading distributions or both were also measured. Flow-straightener systems, some designed to include acoustic treatment in the

baffles, and other flat vanes and louvers were tested in straight-through (nonturning) flow configurations. Vane cascades were studied at flow-turning angles up to 90°. The effect of such other parameters as chord-to-gap ratio and hinge-gap sealing were also evaluated. These tests were conducted over a range of Reynolds numbers (based on chord) from 2×10^5 to 17×10^5 .

The results of this experimental program do not constitute a complete and final treatment of the aerodynamic performance of all flow-control systems any more than did previous work on the subject. These data should, however, contribute to the body of knowledge on the subject and provide additional information useful in optimizing internal flow systems as dictated by complexity, cost, and performance.

The authors wish to express their gratitude to Mr. Daniel J. Clasen and Mr. C. Gary Welling of Sverdrup Technology, Ames Division (formerly Arnold Research Organization, Inc.), for their valuable contributions to this study and for their assistance in the operation of the model and acquisition and reduction of the data.

FLOW CONTROL COMPONENTS

Although there are many kinds of flow-control devices, this study considered only three: flow straighteners, louvers, and turning vanes. The following discussion explains the scope and meaning of these component classes as used in this report.

Flow Straighteners

Flow straighteners are designed to do just what their name implies — straighten the flow in a duct. They reduce or

*Aeromechanics Laboratory, U.S. Army Aviation R&D Command, Ames Research Center, Moffett Field, California 94035.

†Sverdrup Technology, Ames Division, Ames Research Center, Moffett Field, California 94035.

eliminate flow angularities and large-scale turbulence. They are located in a straight, constant-area duct and may straighten flow in two planes, with an egg-crate geometry, or only in one plane with spaced, "two-dimensional" panels. Their inlet face is in a plane perpendicular to the mean entering flow. Significant parameters affecting the losses of flow-straightener systems include flow blockage, cell geometry, and surface roughness.

Louvers

As used in this report, louvers may serve some of the same functions as flow straighteners but are intended as open-closed valving devices. They are usually spaced so as to minimize the blockage they present in the open position. They may also be "racked," that is, have the plane of their leading edges at some nonperpendicular angle to the entering flow. Parameters influencing the losses of louvers include shape, blockage (in these tests corresponding to and controlled by the chord-to-gap ratio), and surface roughness.

Turning Vanes

Turning vanes guide flow uniformly around bends, thus minimizing the corner losses. For the current study, these bends were at angles up to 90° . Most of the vane systems tested were designed to allow a change in flow direction by repositioning a segment of each vane of the cascade. In some cases, one of the directions was straight-through, so that the turning vanes in their 0° turning mode appeared much as louvers, but with closer spacing. In other cases, adjustable flaps or tails were added to fixed, 90° turning vanes. In these latter cases some net turning angles were less than 90° — as low as 0° — with the flow turned 90° by the fixed vane and then turned back again by the tails through an additional bend angle of up to 90° . This compound type of turning vane is not recommended, for it has an unnecessarily high loss, but it was studied as a potentially low-cost modification to existing systems for special purposes.

COMPONENT AERODYNAMIC PERFORMANCE

The aerodynamic performance of the flow straighteners, louvers, and turning vanes was measured in terms of the pressure losses caused by the component, the chord-wise pressure distributions (loads) on the vanes, and the overturn/underturn angles of the flow exiting the vane systems.

Form and Function

Vane-loading distributions, presented as pressure coefficients, can be used to calculate design structural loads for the system. Vane-turning angles can assist in determining the proper or optimum alignment of the vane cascade. The total pressure loss of duct components is of interest and concern from power and energy standpoints because of its linear contribution to the required operating power for a duct or wind-tunnel system (Eckert et al., 1976):

$$P = \frac{(\sum \Delta p_T/q_0) \rho_o^2 A_o^2 V_o^3}{2 \rho_d \eta_d}$$

Here, $\sum \Delta p_T/q_0$ is the sum of the total pressure losses of the several components of the duct system. Of these three aerodynamic performance indicators — vane-loading distribution, turning angle, and total pressure loss — the pressure loss was, in this study, both the most important and the most difficult to measure.

Theoretical Considerations

The total pressure loss for an individual component is the difference in the values of the average total pressures upstream and downstream of the component. Although total pressure is generally easy to measure in discrete locations, getting an accurate integrated measurement across an entire duct cross section is extremely difficult. The difficulty arises from the necessity of taking careful measurements in all flow regions of the duct, including the boundary layer and corners. This task requires a great quantity of data, even to approximate a true integrated average. And when, as in this application, the requirement is for a change in total pressure between two cross sections, the difficulty is compounded.

However, the loss measurement can be made in another and simpler way. For nonrotating flow the static pressure is constant across a plane perpendicular to the flow direction. Thus, static pressure may be determined by only a single sample at a given cross section. Therefore, since the pressure loss can be related to static pressure measurements, the process of loss determination is relatively simple. For incompressible flow the loss is

$$\begin{aligned} \frac{\Delta p_T}{q_1} &= \frac{p_{T_1} - p_{T_2}}{q_1} = \frac{p_{s_1} + q_1 - (p_{s_2} + q_2)}{q_1} \\ &= \frac{p_{s_1} - p_{s_2}}{q_1} + \frac{q_1 - q_2}{q_1} \end{aligned}$$

and, applying continuity considerations where $\rho_1 A_1 V_1 = \rho_2 A_2 V_2$ and $q = 1/2 \rho V^2$,

$$\frac{\Delta p_T}{q_1} = \frac{p_{s1} - p_{s2}}{q_1} - \frac{\rho_1 - \rho_2}{\rho_2}$$

Finally, for measurements taken far enough downstream that all mixing has taken place, the density change across a component is small. Thus,

$$\frac{\Delta p_T}{q_1} = \frac{p_{s1} - p_{s2}}{q_1}$$

Hence, measuring the static pressure drop across a component gives a reasonable approximation of the total pressure loss.

MODEL TEST PROGRAM

The experimental program was carried out on the basis of the theoretical considerations discussed above. The studies included measurements on 3 flow-straightener configurations, 2 louver systems, and 13 turning vane cascades (3 at 0° turning angles).

Apparatus

The duct system used in this test program is shown in figure 1. Dimensions and geometry of the basic apparatus (i.e., without the flow-control component test subject) are given in table 1. The entire duct system was located and operated in an extremely large but fully-enclosed test chamber.

The test apparatus was a simple, nonreturn duct powered by a fixed-pitch, variable-speed fan located at its exit. The duct cross section was rectangular except for the fan shroud and its upstream transition. Both the duct inlet upstream of the test subject and the fan inlet were protected by honeycomb flow straighteners to maximize the quality (uniformity) of the flow entering these two components. The relative position of the inlet duct and settling duct, that is, their spacing and the angle between their longitudinal centerlines, depended on the size and configuration of the component being tested. The detailed geometries of the several configurations tested are shown in the figures along with the presentation of the data they produced.

Instrumentation

All performance data were taken as pressures, using a multiple-tube manometer; data were recorded photographically. The pertinent measuring locations are shown in figure 2. Static pressure taps distributed along the upper surface of the duct, both upstream and downstream of the test component, measured the pressure losses. A traversing pitot-static direction probe (fig. 3) measured turning angles near the center of the duct and at a point about 1 chord length downstream of the cascade exit plane.

Calibration and Accuracy

The traversing survey probe (fig. 3) was calibrated in the 7- by 10-Foot Wind Tunnel (No. 1) at Ames Research Center. The flow angularity parameters were calibrated as functions of indicated, nondimensional pressure differences measured by the multiport direction probe. The probe was tested in upright and inverted orientations, and angles were measured with an inclinometer; a pre-calibrated standard probe was used as a reference.

All pressure readings used for the data presented herein were accurate to about ± 0.5 mm (± 0.02 in.) of vertical water column height. All pressure port locations were known to within about ± 2.5 mm (± 0.1 in.). The duct geometry dimensions were accurate to about ± 1.5 mm (± 0.06 in.) and 0.5° . Vane settings were accurate within $\pm 0.25^\circ$. The uncertainty in pressure loss coefficient, determined by the method of Kline and McClintock (1953), is shown in figure 4.

The combined effect of calibration, installation, and measurement errors in the exit flow-turning angle was $\pm 0.7^\circ$.

Test Procedure

Test components were installed between the upstream inlet and downstream settling ducts. The drive speed of the drive fan was set and held constant while the data were taken. The fan speed was then changed to a new setting (i.e., a new component Reynolds number) and data were taken again. When this process was complete, the test component was exchanged for another and the test procedure was repeated.

These studies considered only steady-state performance characteristics of the components. No attempt was made to determine the effects of gusts or oscillatory flows.

Data Reduction Procedure

The total pressure losses of the component were assumed equal to the measured static pressure losses, consistent with the above discussion (Theoretical Considerations). These losses were determined by taking the differences or offsets in the upstream and downstream pressure distributions, as was done by Miller (1971). Figure 5 shows how the upstream and downstream distributions were extrapolated to the location of the longitudinal centerline of the subject component. These extrapolations were based on the measured slope of the pressure distribution in the empty duct, which is also shown in figure 5. By this process, the losses of the duct were removed from the result, leaving only the losses of the straightener, louver, or vane component.

For some test subjects the inlet and exit duct areas were not equal. In those cases, static pressure measurements indicated a misleading pressure difference caused by the component. Therefore, to keep all reported losses on the same basis, that is, nondimensionalized by q_1 (the dynamic pressure upstream of the component), the indicated pressure differences were adjusted to compensate for the area change:

$$\frac{\Delta p_T}{q_1} = \frac{p_{s1} - p_{s2}}{q_1} + \left[1 - \left(\frac{A_1}{A_2} \right)^2 \right]$$

The overturn/underturn angles of flow-exiting turning-vane systems were measured by the survey probe at several lateral locations in the central region of the duct. The several measurements were then averaged.

RESULTS AND DISCUSSION

Detailed results of the experimental program and sketches of the 11 component styles are presented in figures 6 through 16. A configuration plotting index is provided in table 2. Generally, the flow-control devices are presented in order of increasing turning angle, with flow straighteners, louvers, and 0° turning-angle vanes appearing first. Flow-straightener performance is shown in figures 6 through 8; louver data are given in figures 9 and 10; and turning-vane characteristics are presented in figures 11 through 16.

Plotted component loss results are presented as functions of Reynolds number. Overturn angles for turning-vane configurations are tabulated as mean values. (Although the angularity results are not as consistent and accurate as the pressure losses, they are included in the interests of providing approximate information where no such information has been generally available in the literature.)

A less detailed summary of the experimental results is compiled in table 3 for nonturning devices, in table 4 for 45° turning-vane cascades, and in table 5 for 90° turning devices.

Some analysis of results can be achieved by considering the basic data figures. Some effects are better shown on summary figures. Table 6 is a plotting index for the summary analyses, which are presented in figures 17 through 21.

The experimental results for flow straighteners include the effects of blockage and chord-to-gap ratio, surface condition, and fairing contour.

Considering figures 6-8, it is clear that pressure loss varies with Reynolds number and with blockage (and with chord-to-gap ratio, since blockage and chord-to-gap ratio were coupled through the number of vanes used in a fixed duct size). The effect of chord-to-gap ratio is shown in figure 17, and there is a clear indication that the greater the blockage (and the chord-to-gap ratio), the stronger a function of Reynolds number is the pressure loss. The vane surface had a significant effect on the loss results; both figures 7 and 8 show that the uniform roughness of the fine-mesh screen caused higher losses than the perforated but smooth surfaces of greater or lesser porosity inserts. Figures 7 and 8 also show, comparing data for similar conditions, as in figure 17, that the faired airfoil contour of figure 8 generated a lower loss than the simpler contour of figure 7.

The louver configurations of figures 9 and 10 show similar kinds of unsurprising results, except, perhaps, that the pressure loss of the nonsymmetrical tail of figure 10 may be a slightly stronger function of Reynolds number than is the loss of the symmetrical tail of figure 9.

The results for turning vanes are more complex than those for nonturning devices. Of particular interest are the effects of the following on pressure losses: basic vane contour, total turning angle and tail deflection angle, chord-to-gap ratio, and hinge-gap seals.

Some inferences can be drawn on the effects of basic contour by comparing figures 11(m) and 15 for 90° turns and figures 11(l) and 14(d) for 45° bends. For 90° turns the gradual bend of the multiple-circular-arc airfoil of figure 15 produces much lower losses than the abrupt flow direction changes of the two-segment vane of figures 11(e) and 11(m). However, for 45° turns, if done correctly (i.e., gradually) a series of flat panels (fig. 11(d)) can give a lower loss than a contoured vane such as that shown in figure 14(b); that is, the loss shown in figure 11(l) is lower than that shown in figure 14(d).

Figure 18(a) combines relevant data from figures 11, 15, and 16 to show the effect of total turning angle on the

pressure loss. The circular symbols in figure 18 designate the results for thin, hinged-panel vanes covering the range from 0° to 90° ; the loss increases approximately parabolically with turning angle. The square symbols designate similar data points for the multiple-circular-arc vanes, with tails providing total turning from 90° to 180° . For both the thin-vane and multiple-circular-arc-vane types the variation in turning angle was achieved by tail deflection, and figure 18(b) shows reasonable correlation of loss with tail-deflection angle, regardless of the very different bend angles of the upstream pieces of the two vane types.

A clear pattern of pressure loss variation with chord-to-gap ratio for 45° turns is shown in figure 19(a) and for 90° turns in figure 19(b). Both curves are quasi-parabolic with minimum losses shown between chord-to-gap ratios of 2.5 to 3.0.

The effects of sealing the hinge-gaps between movable vane panels can be seen in figures 11(g) and 11(i) for thin, 45° vanes, and in figure 16(d) for the more complex multiple-turn, over- 90° system. Figure 18 shows, by the difference between the open and solid symbols, that sealing hinge-gaps can significantly flatten the pressure-loss-versus-turning-angle curves.

The final performance indicator considered in this study was the flow overturn angle, measuring the vane's flow-turning efficiency. Figures 20 and 21 show flow overturn angles for two types of vanes. Figure 20, for multiple-circular-arc vanes with tail deflections at 90° , shows greater underturn for greater tail deflection, that is, decreasing tail effectiveness. Figure 21, for thin vanes at 45° and 90° over a range of chord-to-gap ratio, shows increasing turning

effectiveness with increasing chord-to-gap ratio. An overturn angle of 0° was achieved at a chord-to-gap ratio between 2.5 and 3.0.

CONCLUSIONS

There are as many performance results for flow-control devices as there are devices. The documentation and tabulation of pressure loss, pressure distribution, and flow angularity information from this experimental study will contribute to the general body of knowledge of the subject and should prove valuable in future wind-tunnel developmental projects. For lowest losses the components should be developed with the following features in mind: (1) flow-straightening devices should be as aerodynamically contoured with as low a blockage as is practical for the particular application; (2) surface openings, if necessary, say for acoustic treatment, should be accomplished with smooth, perforated plates; (3) turning vanes should be gently curved, not made up of flat panels, and should be spaced at a chord-to-gap ratio of about 3; and (4) any hinge gaps should be sealed.

Other configurations and arrangements will work, of course, but will be less energy-efficient. Should cost efficiency dictate "the simpler approach" to component design, this compilation can help assess the attendant operational and technical penalties.

Ames Research Center

National Aeronautics and Space Administration
and

Aeromechanics Laboratory

AVRADCOM Research and Technology Laboratories
Ames Research Center, Moffett Field, Calif. 94035,
September 21, 1982

REFERENCES

- Eckert, William T.; Mort, Kenneth W.; and Jope, Jean: Aerodynamic Design Guidelines and Computer Program for Estimation of Subsonic Wind Tunnel Performance. NASA TN D-8243, 1976.
- Idel'chik, I. E.: Handbook of Hydraulic Resistance. Coefficients of Local Resistance and of Friction. AEC-TR-6630, The Israel Program for Scientific Translations Ltd., 1966. (Available from Clearinghouse for Federal Scientific and Technical Information, U.S. Department of Commerce.)
- Kline, S. J.; and McClintock, F. A.: The Description of Uncertainties in Single Sample Experiments. Mech. Eng., vol. 75, no. 1, Jan. 1953, pp. 3-8.
- Miller, Donald S.: Internal Flow: A Guide to Losses in Pipe and Duct Systems. British Hydromechanics Research Association, Cranfield, England, 1971.
- Mort, Kenneth W.; Kelly, Mark W.; and Hickey, David H.: The Rationale and Design Features for the 40- by 80-/80- by 120-Foot Wind Tunnel. Paper 9, AGARD Conference Proceedings 174 on Windtunnel Design and Testing Techniques, AGARD CP-174, Mar. 1976.
- Mort, Kenneth W.; Soderman, Paul T.; and Eckert, William T.: Improving Large-Scale Testing Capability by Modifying the 40- by 80-Foot Wind Tunnel. J. Aircraft, vol. 16, no. 8, Aug. 1979, pp. 571-575.

TABLE 1.— DUCT GEOMETRY

Duct segment	Dimension, cm (in.)
Inlet honeycomb	
Cell size	1.3 (0.5)
Length	25.4 (10)
Entrance duct	
Height	91.4 (36)
Width	91.4 (36)
Length	
Minimum	91.4 (36)
Maximum	152.4 (60)
Settling duct	
Height	91.4 (36)
Width	
Minimum	91.4 (36)
Maximum	129.8 (51)
Length	
Minimum	182.9 (72)
Maximum	304.8 (120)
Transition duct	
Honeycomb	
Cell size	1.3 (0.5)
Length	25.4 (10)
Shape transition	
Inlet	91.4 × 91.4 (36 × 36)
Length	91.4 (36)
Exit diameter	121.9 (48)
Fan diameter	121.9 (48)

TABLE 2.— INDEX TO BASIC CONFIGURATION PERFORMANCE FIGURES

Figure number	Component		Flow deflection				Co-plotted configuration variations
	Type	Description	Turning angle, deg		Vane construction		
			Total	Net	Number of segments	Number of hinges	
6	Flow straightener	Egg-crate grid	0	0	1	0	
7	Flow straightener	Flat-sided with acoustic surface	0	0	1	0	Surface roughness, c/g
8	Flow straightener	Streamlined, with acoustic surface	0	0	1	0	Surface roughness, c/g
9	Louver or valve	Symmetrical tail	0	0	1	0	
10	Louver or valve	Nonsymmetrical tail	0	0	1	0	
11	Turning vane	Thin, flat-sided ($t_{\max}/c = 0.021$ to 0.035)	0-90	0-90	1-3	0-2	Chordwise hinge location, Hinge-gap seal, Chord-to-gap ratio, Lower surface fillet
12	Turning vane	Short, thick ($t_{\max}/c = 0.076$)	0, 45	0, 45	1-3	0-2	Lower surface fillet
13	Turning vane	Long, thick ($t_{\max}/c = 0.044$)	0, 45	0, 45	1-3	0-2	Lower surface fillet
14	Turning vane	Thick, flexible nose contour	0, 45	0, 45	1, 2	0, 1	
15	Turning vane	Multiple-circular-arc	90	90	1	0	
16	Turning vane	Multiple-circular-arc with tail	90-180	90-0	2	1	Hinge-gap seal

TABLE 3.- SUMMARY OF RESULTS FOR NONTURNING DEVICES

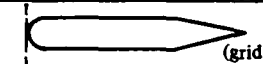



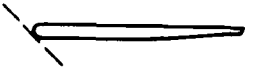

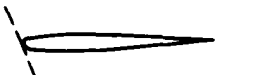
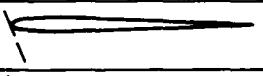

Sketch	Figure number	Blockage	Chord-to-gap ratio, c_v/g	Surface	$\Delta p_T/q_1$ (Rn)
 (grid)	6	61.5	18.5	Smooth	$3.31 (5 \times 10^5)$
 (2D)	7	11.11	1.7	Screen	$.072 (10^6)$
		16.67	2.1	Screen	$.115 (10^6)$
		27.78	3.3	Screen	$.292 (10^6)$
		27.78	3.3	40% porous	$.265 (10^6)$
		27.78	3.3	70% porous	$.275 (10^6)$
 (2D)	8	11.11	1.7	Screen	$.060 (10^6)$
		16.67	2.1	Screen	$.098 (10^6)$
		27.78	3.3	Screen	$.251 (10^6)$
		27.78	3.3	40% porous	$.218 (10^6)$
		27.78	3.3	70% porous	$.224 (10^6)$
	9	4.17	.71	Smooth	$.015 (5 \times 10^5)$
	10	4.17	.71	Smooth	$.012 (5 \times 10^5)$
	11(a,f)	9.72	4.5	Smooth	$.091 (5 \times 10^5)$
	12(a,c)	16.67	2.2	Smooth	$.027 (5 \times 10^5)$
	13(a,c)	16.67	3.7	Smooth	$.055 (5 \times 10^5)$
	14(a,c)	16.67	2.3	Smooth	$.044 (5 \times 10^5)$

TABLE 4.- SUMMARY OF RESULTS FOR 45° TURNING DEVICES

Sketch	Figure number	Blockage	Chord-to-gap ratio, c_v/g	c_h/c	Hinge gap	$\Delta p_T/q_1$ (Rn)	ϕ , deg
	11(b,g)	6.94	2.6	0.4	Sealed	$0.25 (5 \times 10^5)$	2.1
		6.94	2.6	.4	Open	$.50 (5 \times 10^5)$	2.4
		11.81	4.4	.4	Open	$.45 (5 \times 10^5)$	-2
	11(c,i)	2.78	1.2	.5	Sealed	$.07 (5 \times 10^5)$	-2.3
		5.56	2.2	.5	Sealed	$.06 (5 \times 10^5)$	-6
		9.03	3.3	.5	Sealed	$.07 (5 \times 10^5)$.3
		11.81	4.4	.5	Open	$.13 (5 \times 10^5)$	1.0
		11.81	4.4	.5	Open	$.46 (5 \times 10^5)$	1.2
	11(c,k)	5.56	2.2	.5	Sealed	$.06 (5 \times 10^5)$	-3
		9.03	3.3	w/22.5° fillet	Sealed	$.07 (5 \times 10^5)$.5
		5.56	2.2	.5	Sealed	$.05 (5 \times 10^5)$	0
		9.03	3.3	w/34° fillet	Sealed	$.07 (5 \times 10^5)$.4
	11(d,l)	11.81	4.5	0.33 and .67	Sealed	$.11 (5 \times 10^5)$	-1.8
	12(b,d)	16.67	2.1	.4	Sealed	$.40 (5 \times 10^5)$	2.0
	12(b,d)	16.67	2.1	.4 w/22.5° fillet	Sealed	$.40 (5 \times 10^5)$	3.7
	13(b,d)	16.67	3.7	.17	Sealed	$.33 (10^6)$.6
	13(b,d)	16.67	3.7	.17 w/22.5° fillet	Sealed	$.37 (10^6)$	1.1
	14(b,d)	16.67	2.2	.27	Sealed	$.18 (5 \times 10^5)$	3.5

TABLE 5.— SUMMARY OF RESULTS FOR 90° TURNING DEVICES



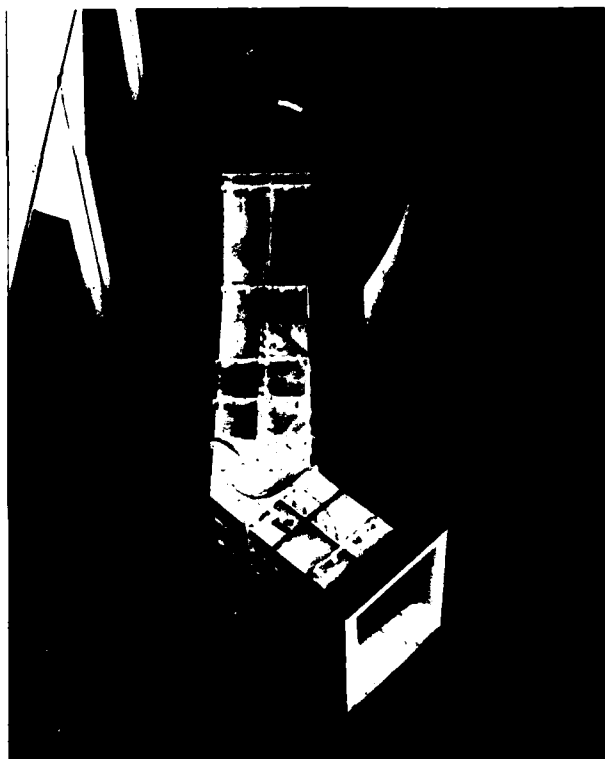
Sketch	Figure number	Blockage	Chord-to-gap ratio, c_v/g	c_h/c	Hinge gap	$\Delta p_T/q_1$ (Rn)	ϕ , deg
	15(b)	27.66	2.0	—	None	$\sim 12 (5 \times 10^5)$	
	16(b)	27.66	4.0	0.48	Open	.15 (5×10^5)	0.8

TABLE 6.— INDEX TO SUMMARY PERFORMANCE FIGURES

Figure number	Effects shown		Component type	Reference figures
	Primary	Secondary		
17	c/g for $\Delta p_T/q_1$	Contour for $\Delta p_T/q_1$	Flow straightener	7(b), 8(b)
18(a)	β for $\Delta p_T/q_1$	Hinge-gap seal for $\Delta p_T/q_1$	Thin and thick vanes	11(f), (i), (m), 15(b), 16(b), (d), (f), (g)
18(b)	θ_t for $\Delta p_T/q_1$			
19	c/g for $\Delta p_T/q_1$		Thin vanes	11(c), (e), (i), (m)
20	θ_t for overturn angle		Multiple-circular-arc vanes	16(b),(d),(f),(g)
21	c/g for overturn angle		Thin vanes	11(i), (m)



(a) Overhead view.



(b) Inlet quadrant view.

Figure 1.— Test duct and apparatus in 45° turning configuration.

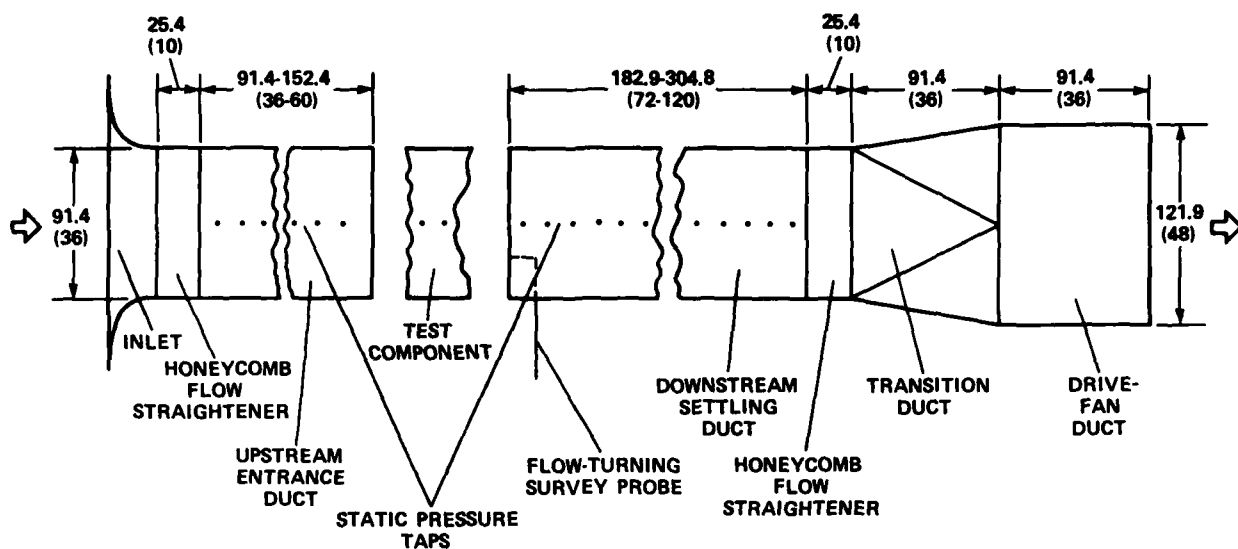


Figure 2.— Duct geometry and pressure-measuring locations.

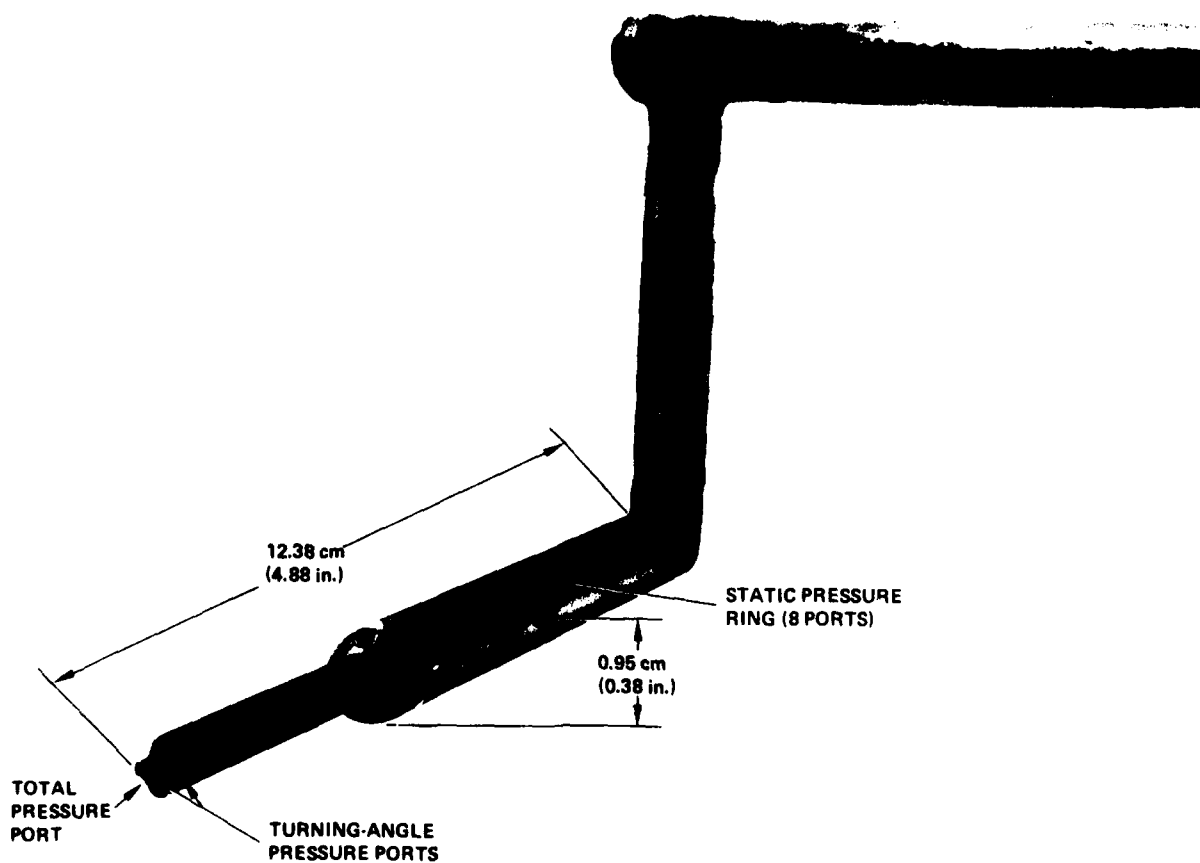


Figure 3.— Flow-turning survey probe.

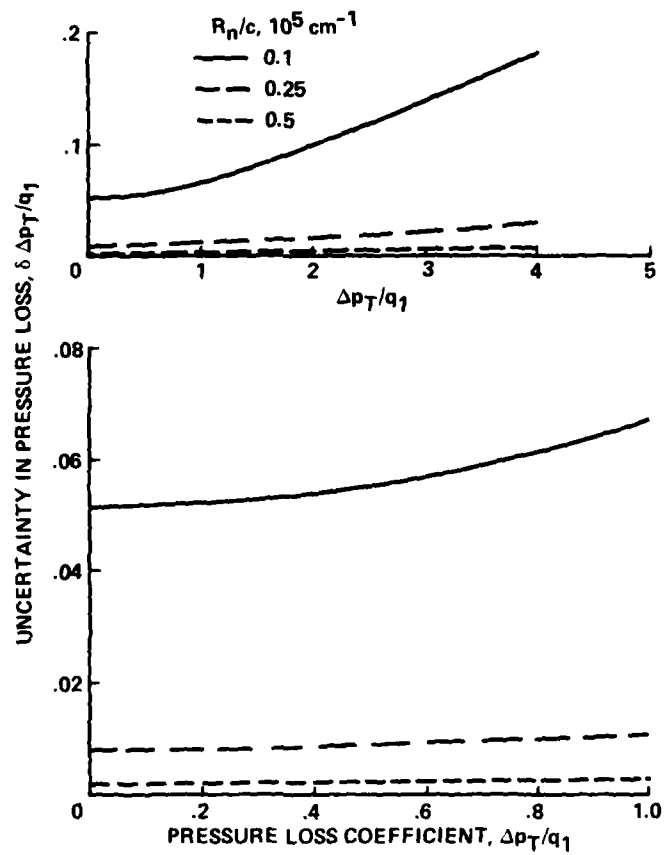
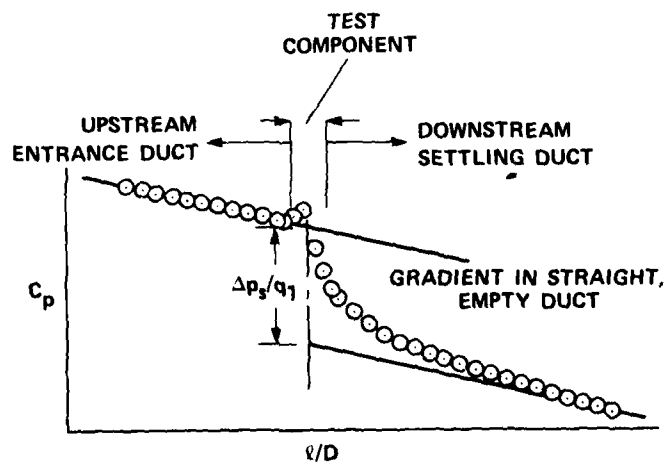
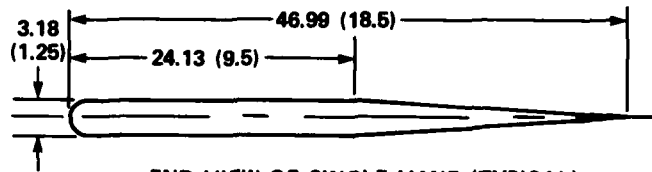


Figure 4.— Uncertainty in pressure-loss results.

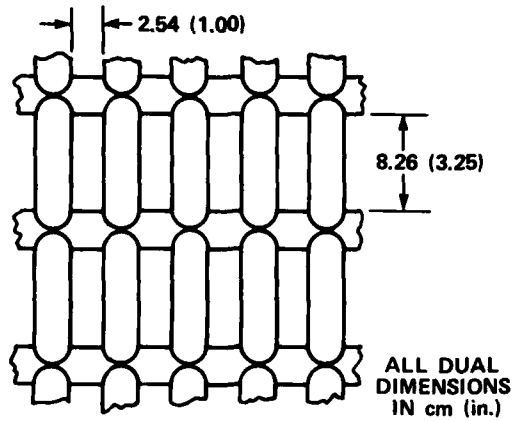


$$\frac{\Delta p_T}{q_1} = \frac{\Delta p_s}{q_1} + \left(1 - \left(\frac{A_1}{A_2} \right)^2 \right)$$

Figure 5.— Schematic of loss-determination technique.

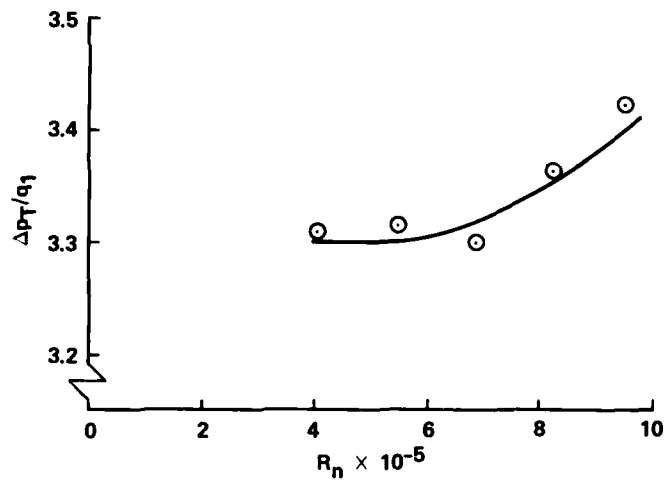


END VIEW OF SINGLE VANE (TYPICAL)



FRONT VIEW OF PORTION OF STRAIGHTENER GRID

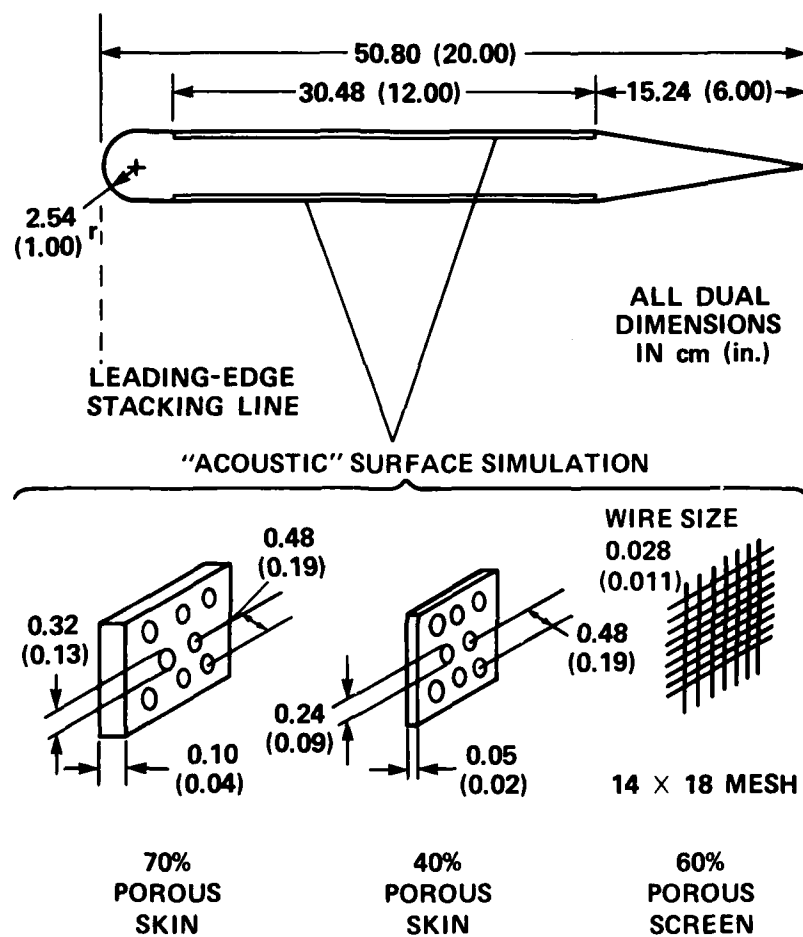
(a) Geometry details.



SYMBOL	CHORD-TO-GAP RATIO, c_v/g	BLOCKAGE, A_B/A_1 , %	COMPONENT AREA RATIO, A_2/A_1	VANE SURFACE
○	18.5	61.5	1.0	SMOOTH

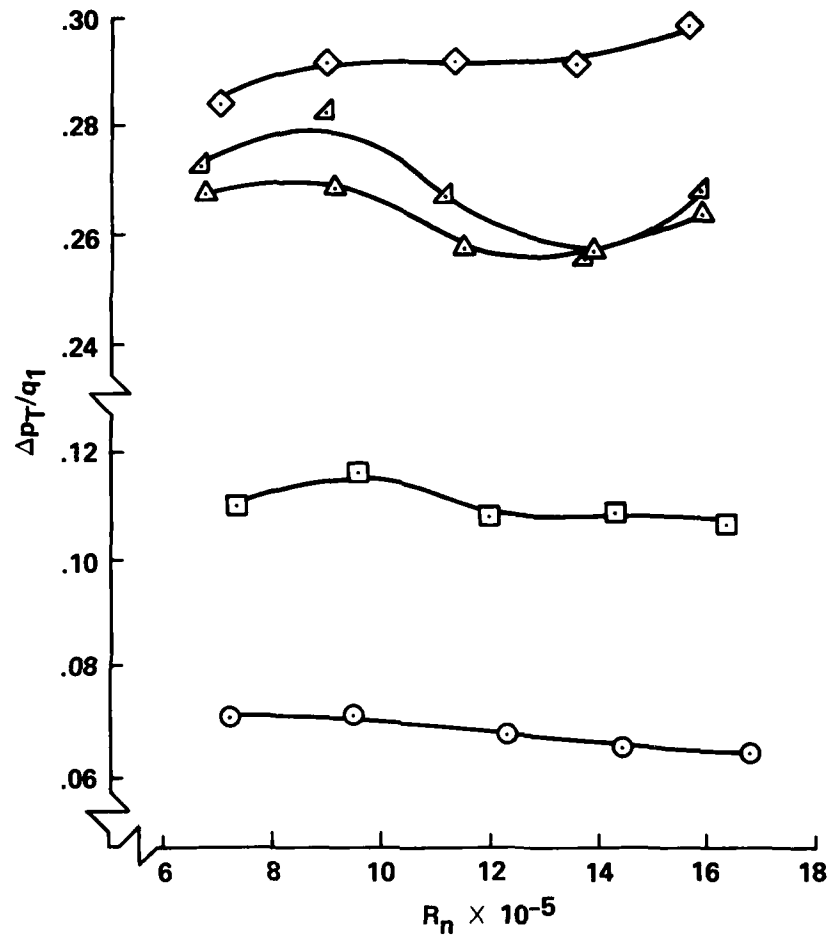
(b) Aerodynamic performance.

Figure 6.— Eggcrate-type flow-straightener grid.



(a) Geometry details.

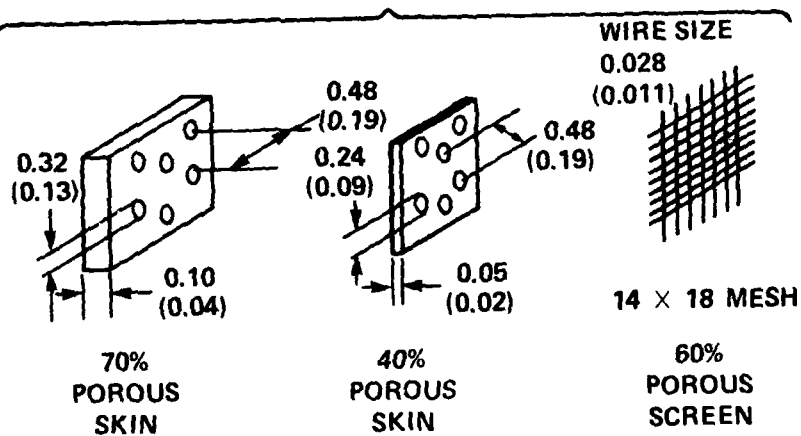
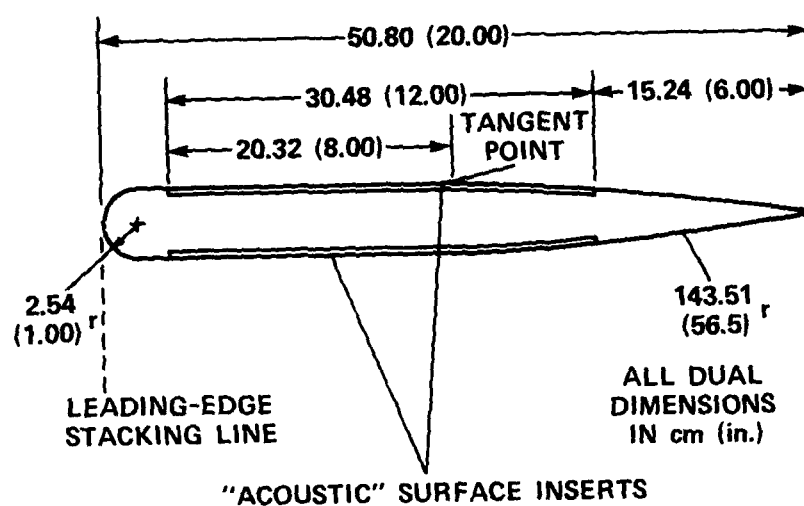
Figure 7.— Flow straighteners with flat, "acoustic" sides.



SYMBOL	CHORD-TO-GAP RATIO, c_v/g	BLOCKAGE, A_B/A_1 , %	COMPONENT AREA RATIO, A_2/A_1	VANE SURFACE POROSITY, %
○	1.7	11.11	1.0	60
□	2.1	16.67	↓	↓
◇	3.3	27.78	↓	40
△	↓	↓	↓	70
▽				

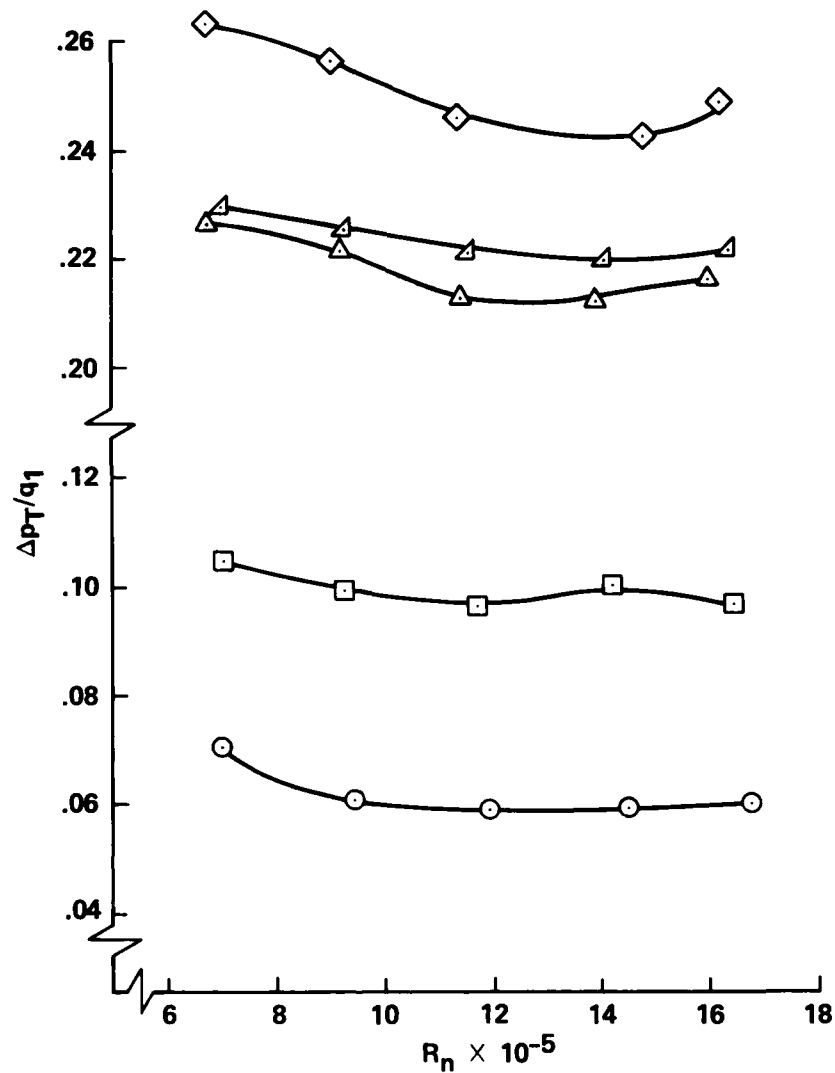
(b) Aerodynamic performance.

Figure 7.— Concluded.



(a) Geometry details.

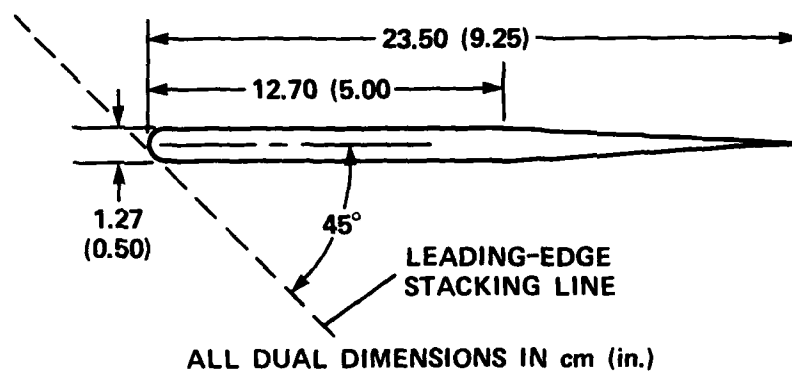
Figure 8.— Flow straighteners with faired, "acoustic" sides.



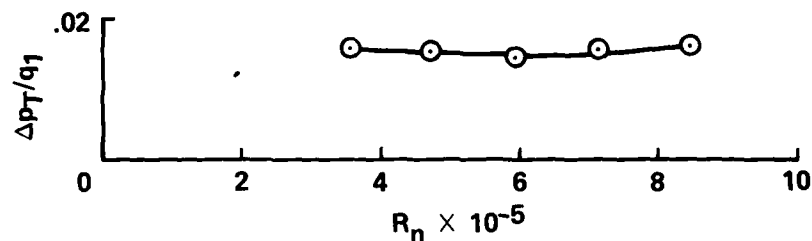
SYMBOL	CHORD-TO-GAP RATIO, c_v/g	BLOCKAGE, A_B/A_1 , %	COMPONENT AREA RATIO, A_2/A_1	VANE SURFACE POROSITY, %
○	1.7	11.11	1.0	60
□	2.1	16.67	↓	↓
◇	3.3	27.78	↓	↓
△	↓	↓	↓	40
▴	↓	↓	↓	70

(b) Aerodynamic performance.

Figure 8.— Concluded.



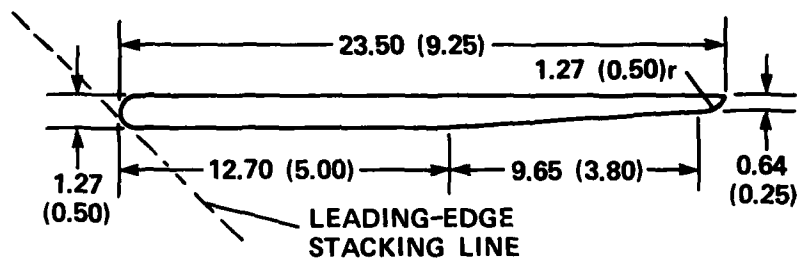
(a) Geometry details.



SYMBOL	CHORD-TO-GAP RATIO, c_v/g	BLOCKAGE, A_B/A_1 , %	COMPONENT AREA RATIO, A_2/A_1
○	0.71	4.17	1.0

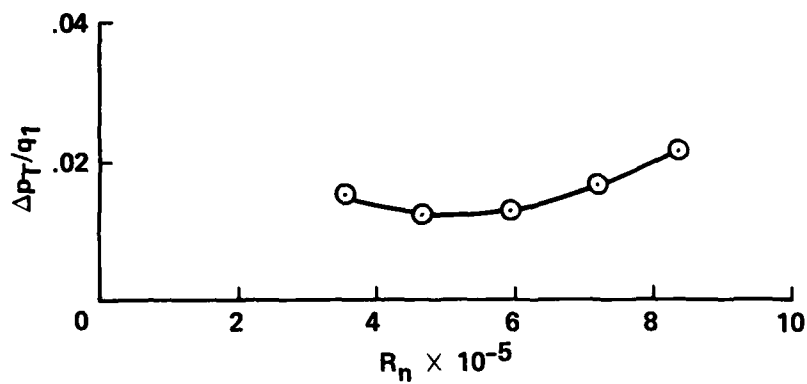
(b) Aerodynamic performance.

Figure 9.— Louvers with symmetrical tails.



ALL DUAL DIMENSIONS IN cm (in.)

(a) Geometry details.



SYMBOL	CHORD-TO-GAP RATIO, c_v/g	BLOCKAGE, A_B/A_1 , %	COMPONENT AREA RATIO, A_2/A_1
O	0.71	4.17	1.0

(b) Aerodynamic performance.

Figure 10.— Louvers with nonsymmetrical tails.

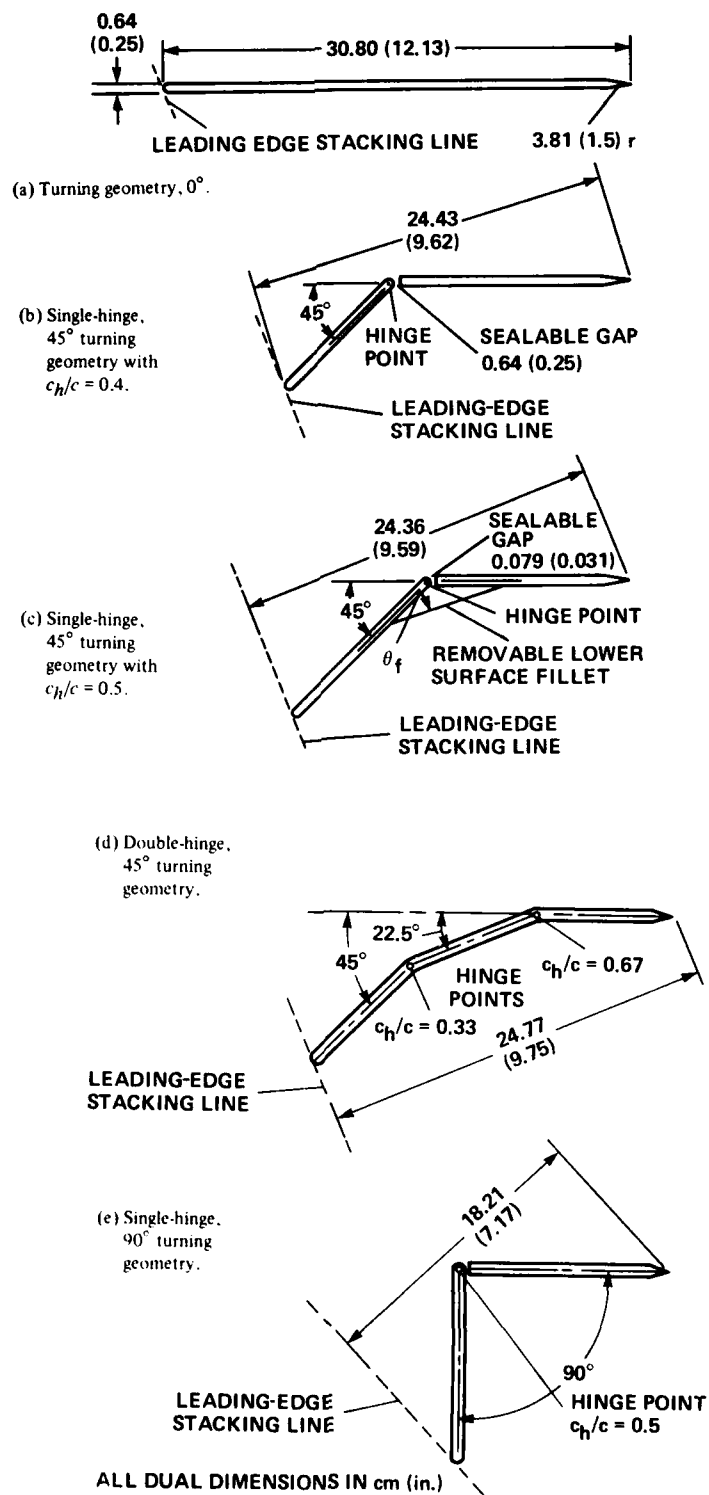
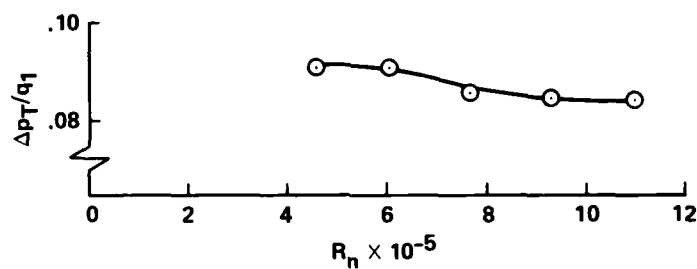
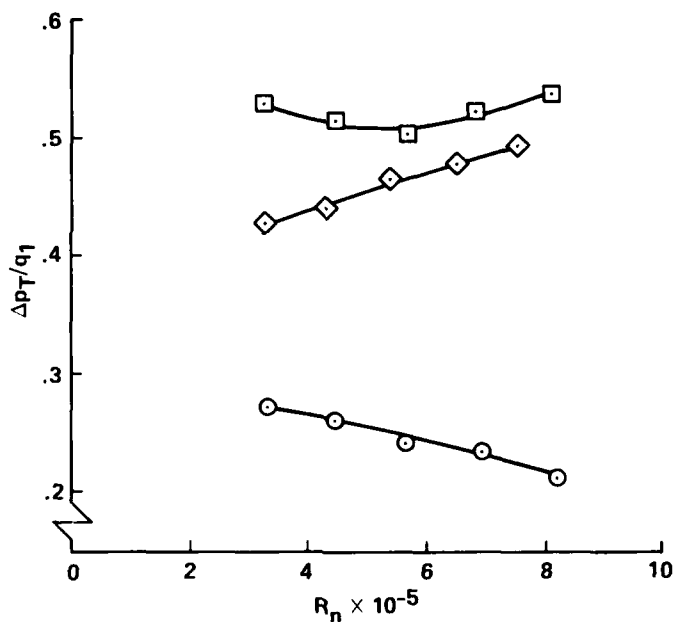


Figure 11.— Variations of thin, flat-sided turning vanes.



SYMBOL	CHORD- TO-GAP RATIO, c_v/g	BLOCKAGE, A_B/A_1 , %	COMPONENT AREA RATIO, A_2/A_1	HINGE GAP
○	4.5	9.72	1.0	NONE

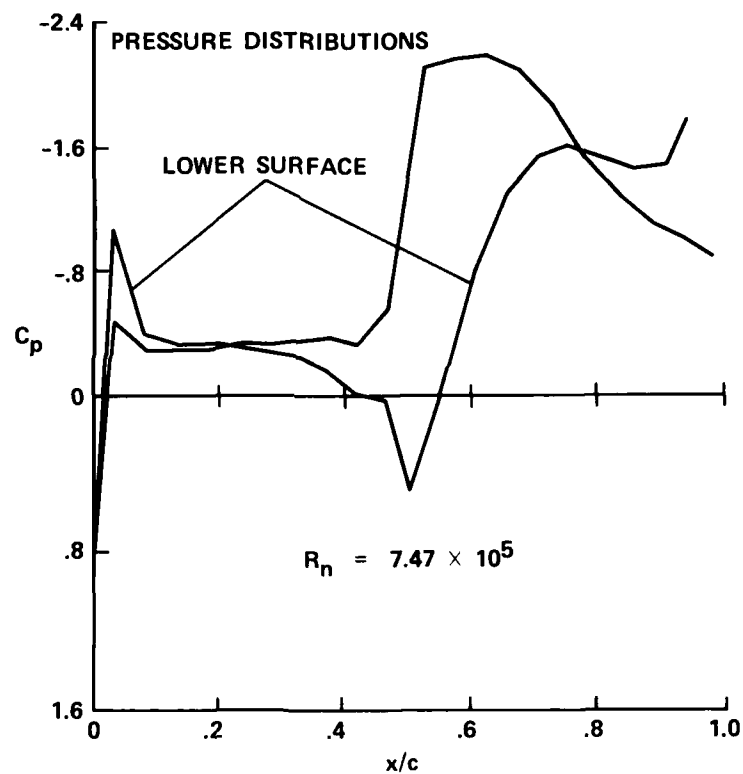
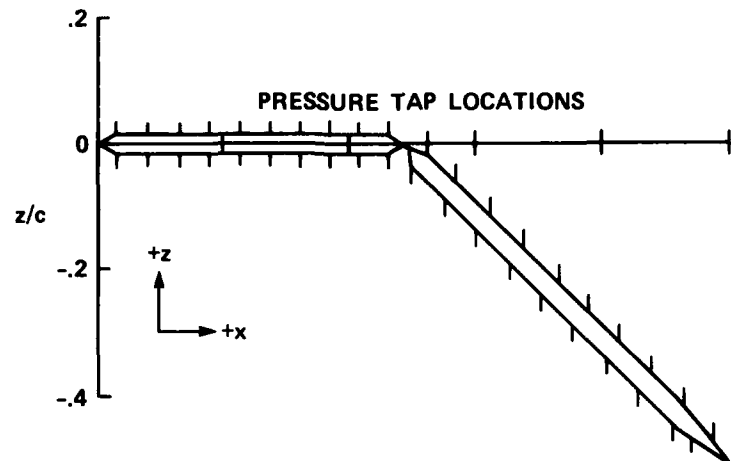
(f) Aerodynamic performance at 0° turning angle (geometry per fig. 11(a)).



SYMBOL	CHORD- TO-GAP RATIO, c_v/g	BLOCKAGE A_B/A_1 , %	COMPONENT AREA RATIO, A_2/A_1	HINGE GAP	FILLET ANGLE, θ_f , deg	OVERTURN ANGLE, ϕ , deg
○	2.6	6.94	1.0	SEALED	NONE	2.1
□	↓	↓	↓	OPEN	↓	2.4
◇	4.4	11.81	↓	↓	↓	-0.2

(g) Aerodynamic performance at 45° turning angle (geometry per fig. 11(b)).

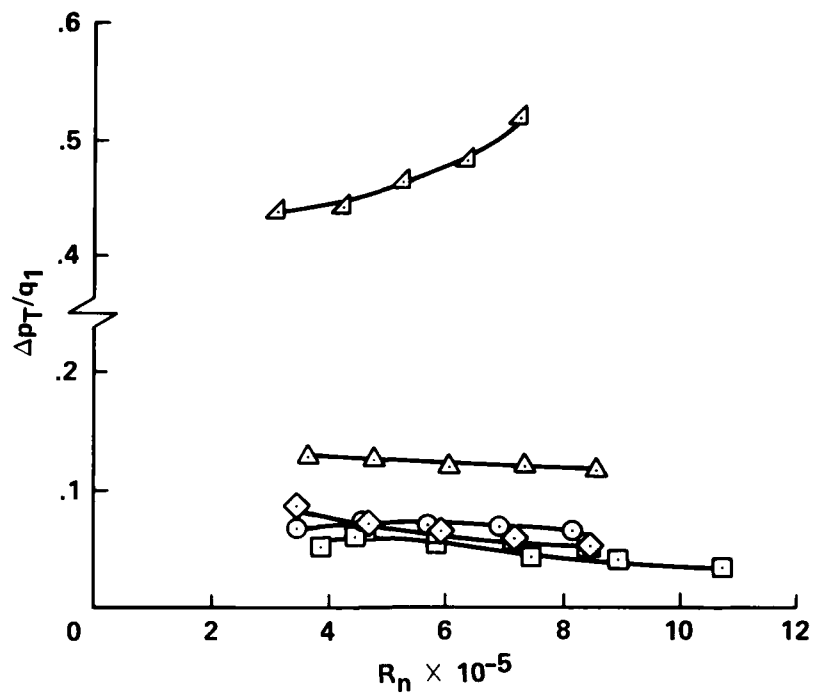
Figure 11.— Continued.



CHORD-TO-GAP RATIO, c_v/g	BLOCKAGE, A_B/A_1 , %	COMPONENT AREA RATIO, A_2/A_1	HINGE GAP	FILLET ANGLE, θ_f , deg
4.4	11.81	1.0	OPEN	NONE

(h) Pressure distributions at 45° turning angle (geometry per fig. 11(b)).

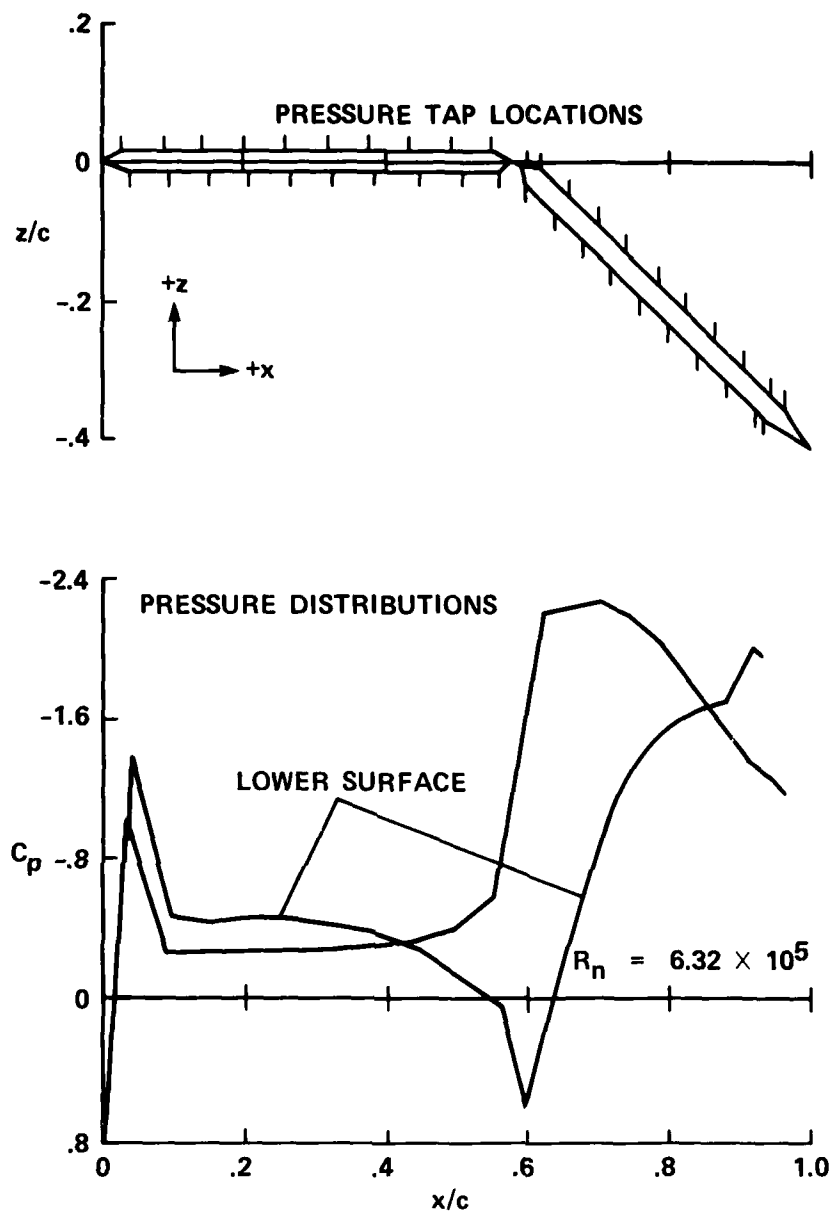
Figure 11.— Continued.



SYMBOL	CHORD-TO-GAP RATIO, c_v/g	BLOCKAGE, A_B/A_1 , %	COMPONENT AREA RATIO, A_2/A_1	HINGE GAP	FILLET ANGLE, θ_f , deg	OVERTURN ANGLE, ϕ , deg
○	1.2	2.78	1.0	SEALED	NONE	-2.3
□	2.2	5.56	↓	↓	↓	-0.6
◇	3.3	9.03	↓	↓	↓	0.3
△	4.4	11.81	↓	↓	↓	1.0
△	↓	↓	↓	OPEN	↓	1.2

(i) Aerodynamic performance at 45° turning angle (geometry per fig. 11(c)).

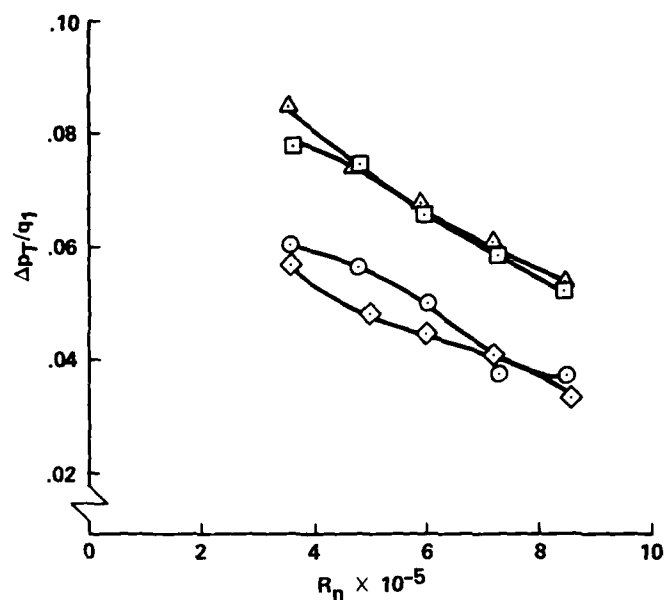
Figure 11.— Continued.



CHORD-TO-GAP RATIO, c_v/g	BLOCKAGE, A_B/A_1 , %	COMPONENT AREA RATIO, A_2/A_1	HINGE GAP	FILLET ANGLE, θ_f , deg
4.4	11.81	1.0	OPEN	NONE

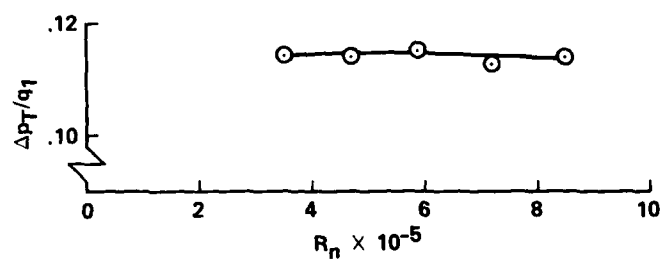
(j) Pressure distributions at 45° turning angle (geometry per fig. 11(c)).

Figure 11.— Continued.



SYMBOL	CHORD-TO-GAP RATIO, c_v/g	BLOCKAGE, A_B/A_1 , %	COMPONENT AREA RATIO, A_2/A_1	HINGE GAP	FILLET ANGLE, θ_f , deg	OVERTURN ANGLE, ϕ , deg
○	2.2	5.56	1.0	SEALED	22.5	-0.3
□	3.3	9.03	↓	↓	↓	0.5
◇	2.2	5.56	↓	↓	34	0.0
△	3.3	9.03	↓	↓	↓	0.4

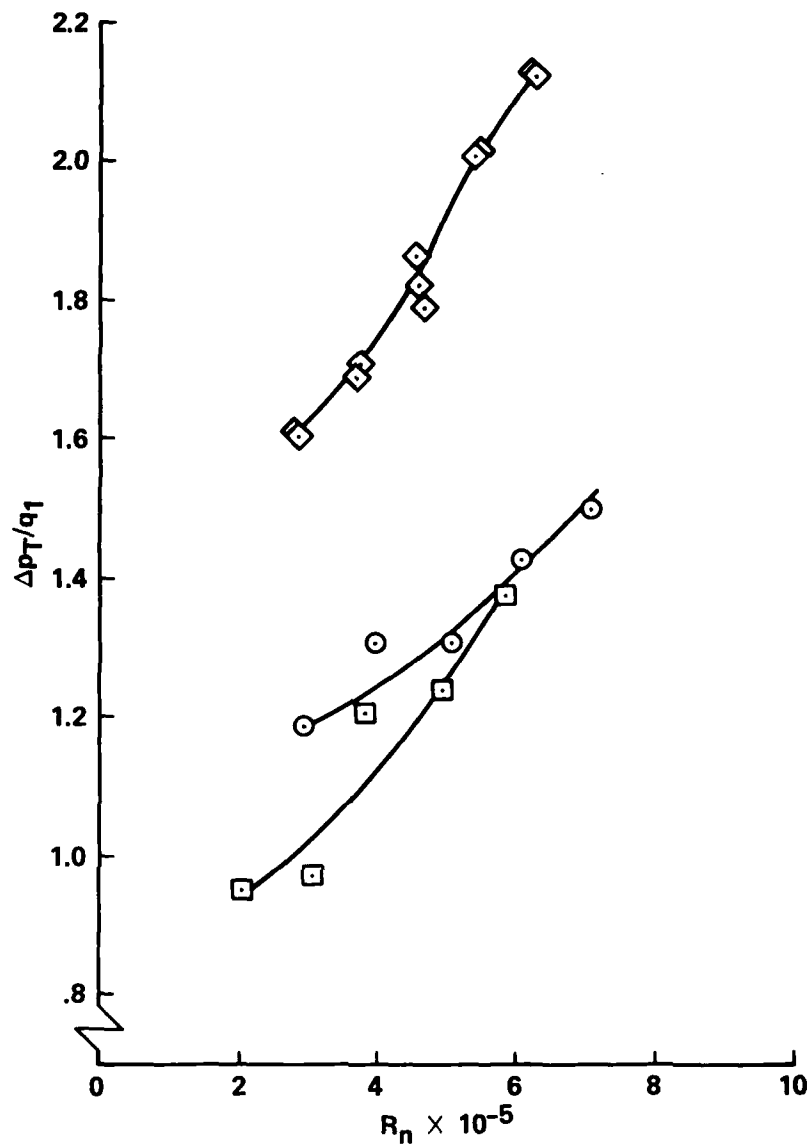
(k) Aerodynamic performance at 45° turning angle with lower surface fillet (geometry per fig. 11(c)).



SYMBOL	CHORD-TO-GAP RATIO, c_v/g	BLOCKAGE, A_B/A_1 , %	COMPONENT AREA RATIO, A_2/A_1	HINGE GAP	FILLET ANGLE, θ_f , deg	OVERTURN ANGLE, ϕ , deg
○	4.5	11.81	1.0	SEALED	RADIUS	-1.8

(l) Aerodynamic performance at 45° turning angle (geometry per fig. 11(d)).

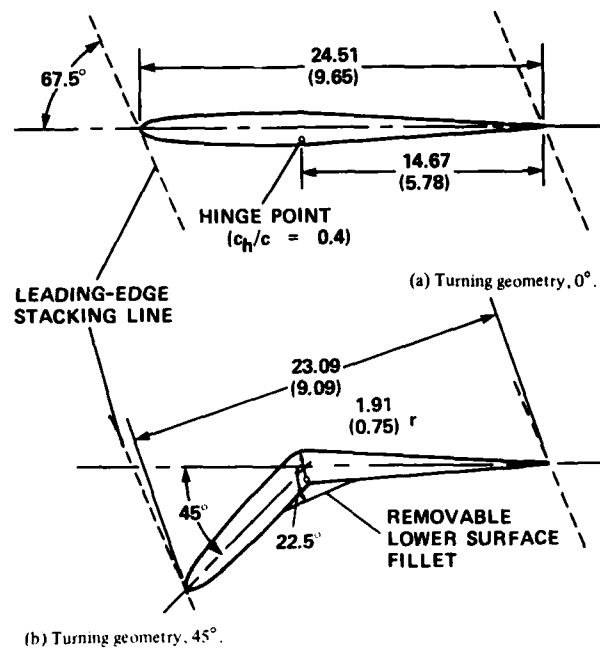
Figure 11.— Continued.



SYMBOL	CHORD-TO-GAP RATIO, c_v/g	BLOCKAGE, A_B/A_1 , %	COMPONENT AREA RATIO, A_2/A_1	HINGE GAP	FILLET ANGLE, θ_f , deg	OVERTURN ANGLE, ϕ , deg
\circ	2.3	11.11	1.0	OPEN	NONE	-6.2
\square	3.0	14.58	\downarrow	\downarrow	\downarrow	0.2
\diamond	4.7	22.22	\downarrow	\downarrow	\downarrow	6.2

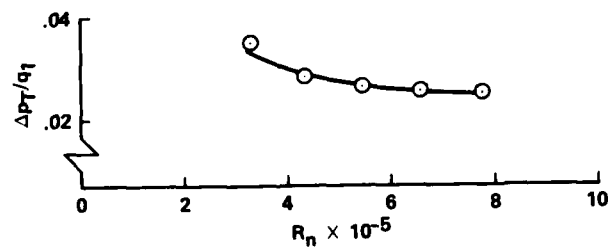
(m) Aerodynamic performance at 90° turning angle (geometry per fig. 11(c)).

Figure 11.— Concluded.



x/c , ($c = 24.51$ cm)	y/c , ($c = 24.51$ cm)
0	0
0.013	0.013
0.025	0.018
0.050	0.024
0.075	0.028
0.100	0.031
0.150	0.035
0.200	0.038
0.300	0.039
0.400	0.038

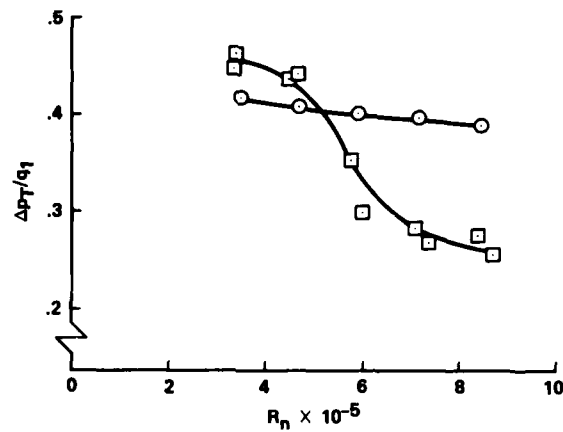
ALL DUAL DIMENSIONS IN cm (in.)



SYMBOL	CHORD-TO-GAP RATIO, c_v/g	BLOCKAGE, A_B/A_1 , %	COMPONENT AREA RATIO, A_2/A_1	HINGE GAP
O	2.2	16.67	1.0	NONE

(c) Aerodynamic performance at 0° turning angle (geometry per fig. 12(a)).

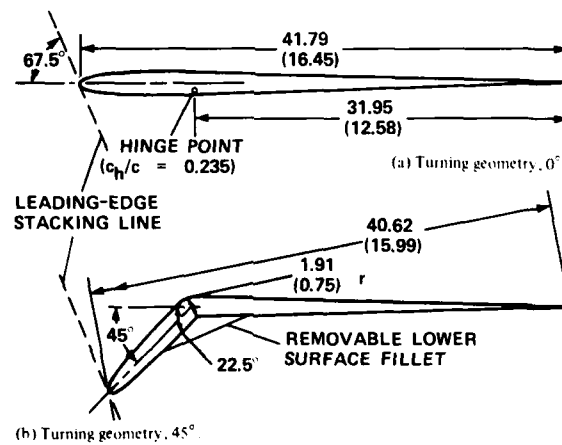
Figure 12.— Variations of short, thick turning vanes ($t_{\max}/c = 0.076$).



SYMBOL	CHORD-TO-GAP RATIO, c_v/g	BLOCKAGE, A_B/A_1 , %	COMPONENT AREA RATIO A_2/A_1	HINGE GAP	FILLET ANGLE, θ_f , deg	OVERTURN ANGLE, ϕ , deg
○	2.1	16.67	1.0	SEALED	NONE	2.0
□	↓	↓	↓	↓	22.5	3.7

(d) Aerodynamic performance at 45° turning angle (geometry per fig. 12(b)).

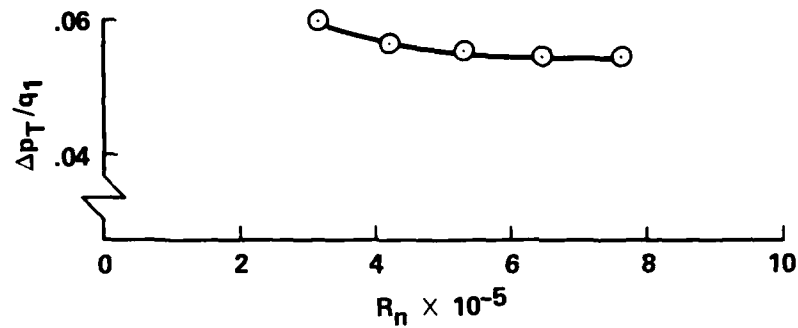
Figure 12.— Concluded.



x/c , ($c = 41.79$ cm)	y/c , ($c = 41.79$ cm)
0	0
0.007	0.008
0.015	0.010
0.029	0.014
0.044	0.017
0.059	0.018
0.088	0.021
0.118	0.022
0.177	0.023
0.235	0.022

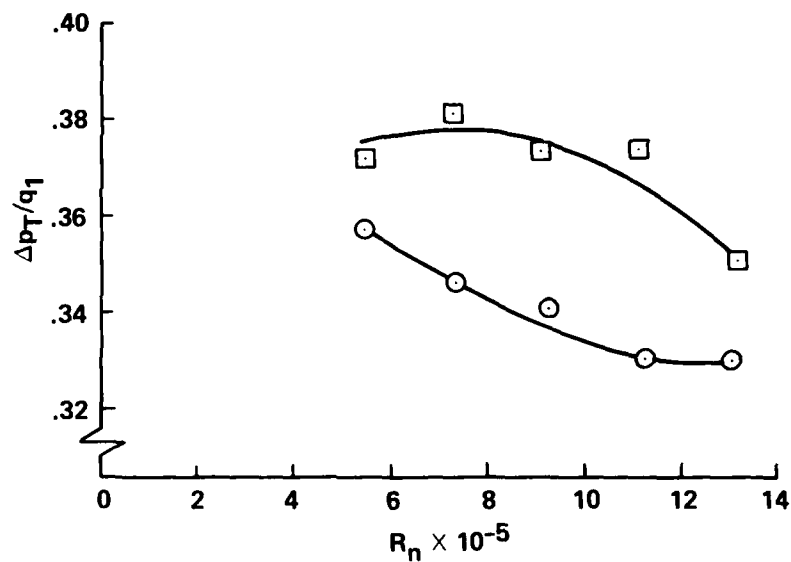
ALL DUAL DIMENSIONS IN cm (in.)

Figure 13.— Variations of long, thick turning vanes ($r_{max}/c = 0.044$).



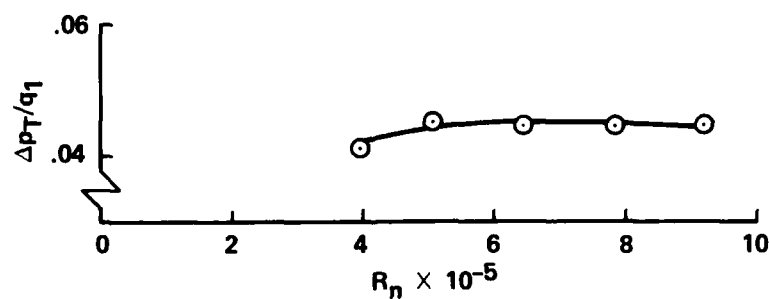
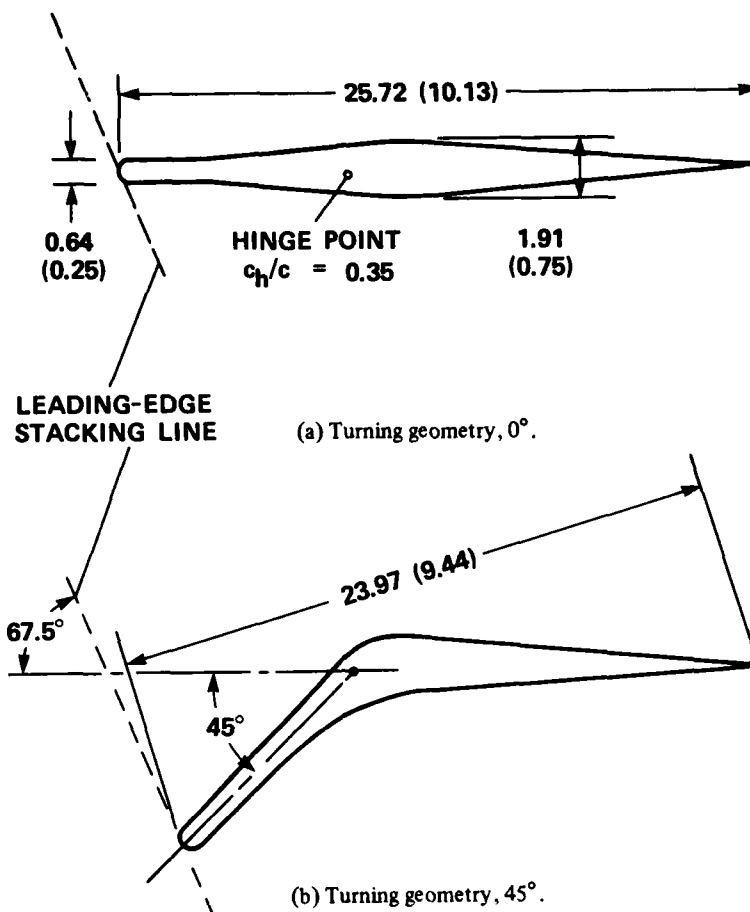
SYMBOL	CHORD-TO-GAP RATIO, c_v/g	BLOCKAGE, A_B/A_1 , %	COMPONENT AREA RATIO, A_2/A_1	HINGE GAP
○	3.7	16.67	1.0	NONE

(c) Aerodynamic performance at 0° turning angle (geometry per fig. 13(a)).



SYMBOL	CHORD-TO-GAP RATIO, c_v/g	BLOCKAGE, A_B/A_1 , %	COMPONENT AREA RATIO, A_2/A_1	HINGE GAP	FILLET ANGLE, θ_f , deg	OVERTURN ANGLE, ϕ , deg
○	3.6	16.67	1.0	SEALED	NONE	0.6
□	↓	↓	↓	↓	22.5	1.1

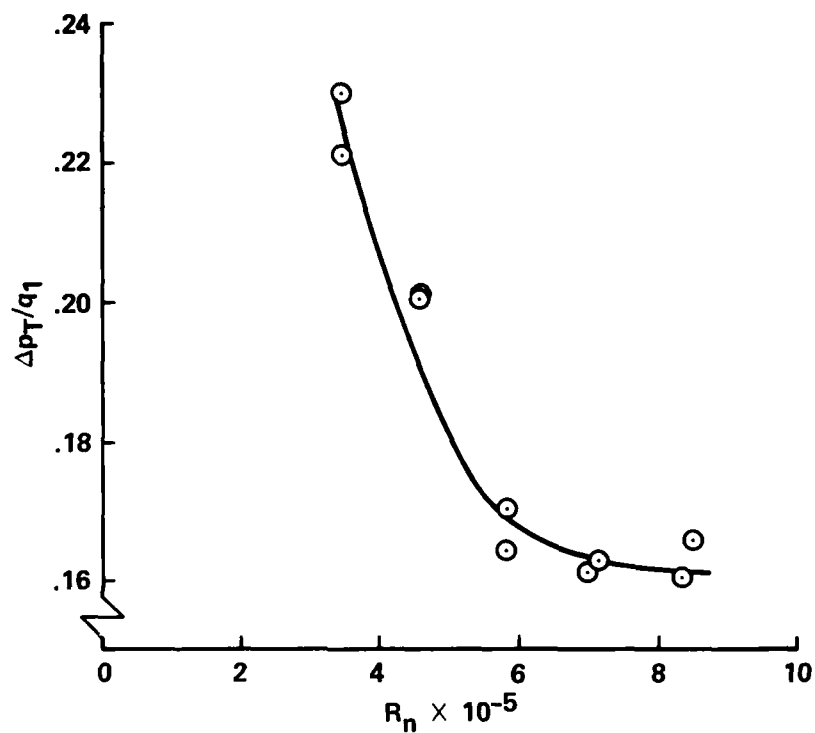
(d) Aerodynamic performance at 45° turning angle (geometry per fig. 13(b)).



SYMBOL	CHORD-TO-GAP RATIO, c_v/g	BLOCKAGE, A_B/A_1 , %	COMPONENT AREA RATIO, A_2/A_1	HINGE GAP
○	2.3	16.67	1.0	NONE

(c) Aerodynamic performance at 0° turning angle (geometry per fig. 14(a)).

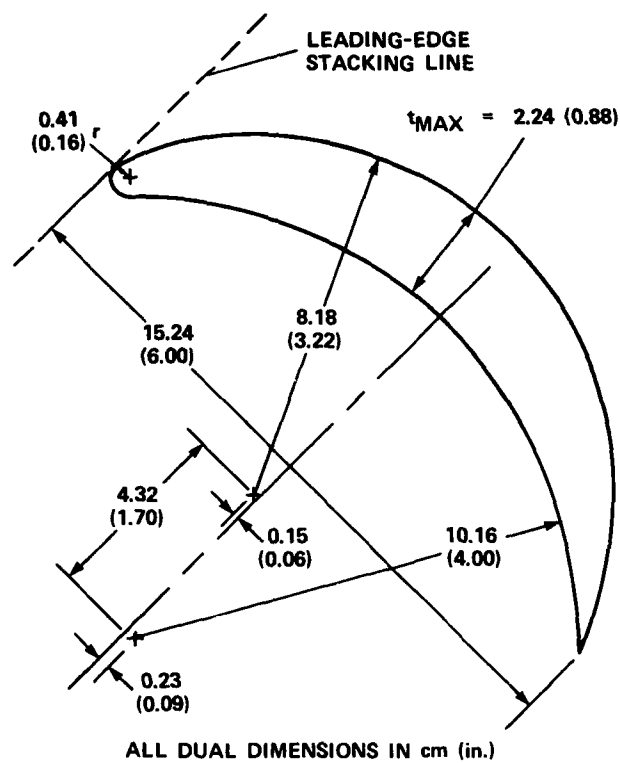
Figure 14.— Variations of thick, flexible-nose turning vanes.



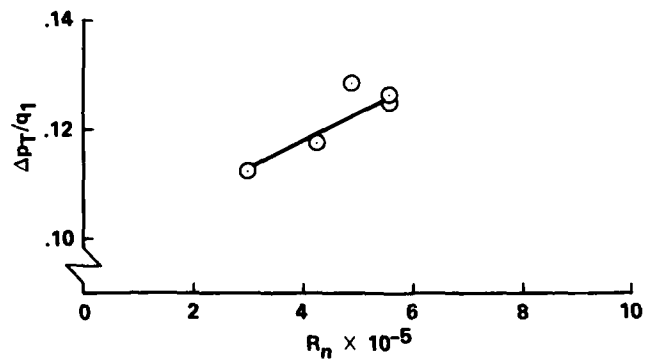
SYMBOL	CHORD-TO-GAP RATIO, c_v/g	BLOCKAGE A_B/A_1 , %	COMPONENT AREA RATIO, A_2/A_1	HINGE GAP	FILLET ANGLE, θ_f , deg	OVERTURN ANGLE, ϕ , deg
○	2.2	16.67	1.0	SEALED	NONE	3.5

(d) Aerodynamic performance at 45° turning angle (geometry per fig. 14(b)).

Figure 14.— Concluded.



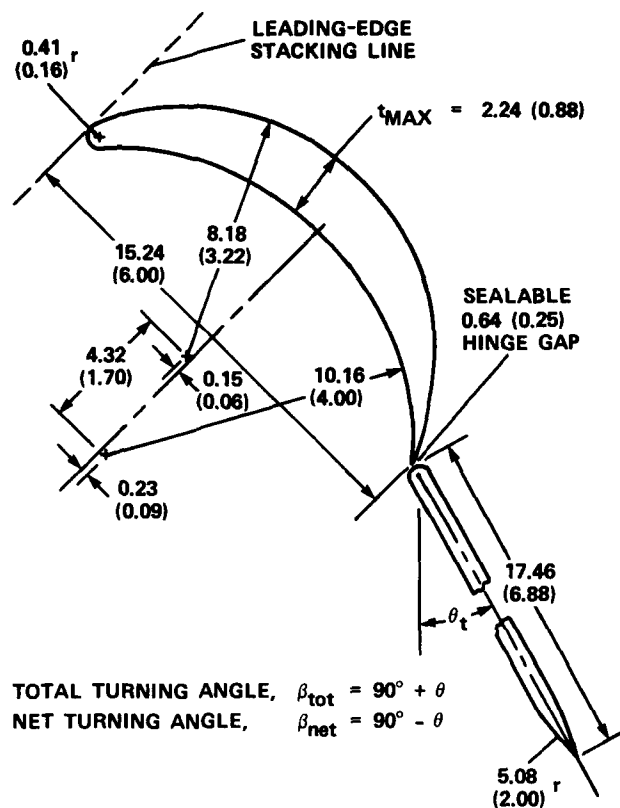
(a) Geometry details.



SYMBOL	CHORD-TO-GAP RATIO, c_v/g	BLOCKAGE A_B/A_1 , %	COMPONENT AREA RATIO, A_2/A_1
O	2.0	27.66	1.0

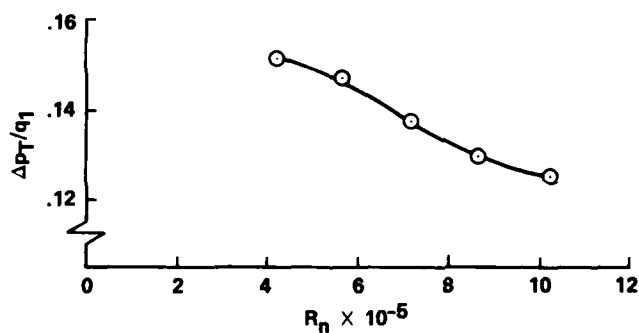
(b) Aerodynamic performance.

Figure 15.— 90° multiple-circular-arc turning vanes.



ALL DUAL DIMENSIONS IN cm (in.)

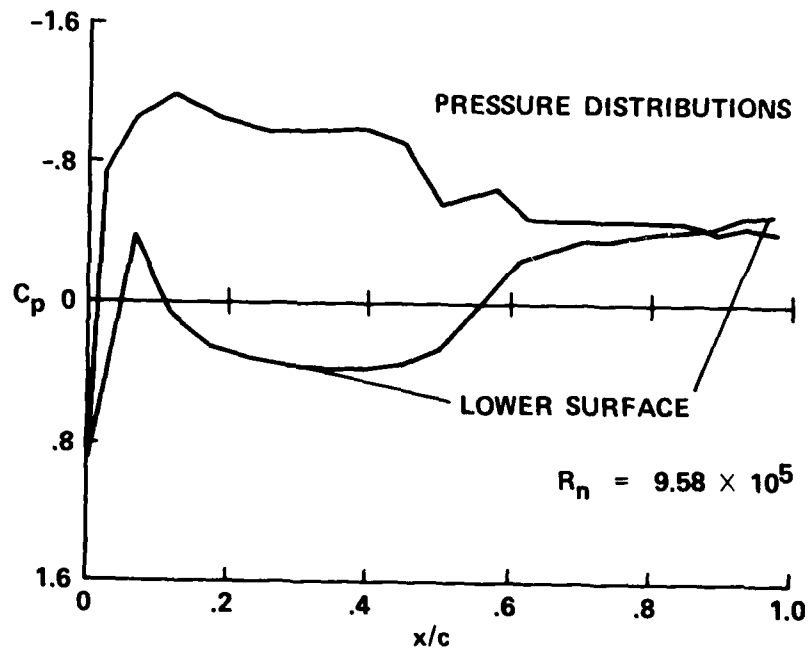
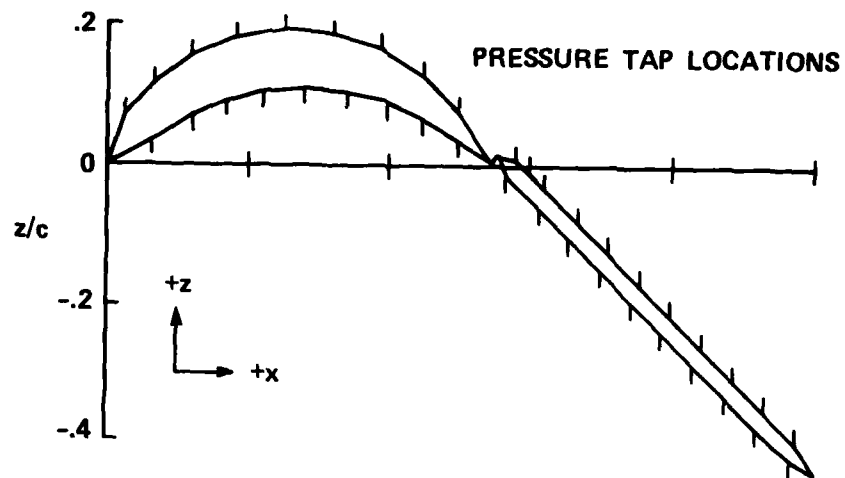
(a) Geometry details.



SYMBOL	CHORD-TO-GAP RATIO, c_v/g	BLOCKAGE, A_B/A_1 , %	COMPONENT AREA RATIO, A_2/A_1	HINGE GAP	FILLET ANGLE, θ_f , deg	OVERTURN ANGLE, ϕ , deg
○	4.0	27.66	1.0	OPEN	NONE	0.8

(b) Aerodynamic performance for $\beta_{tot} = \beta_{net} = 90^\circ$, $\theta_t = 0^\circ$.

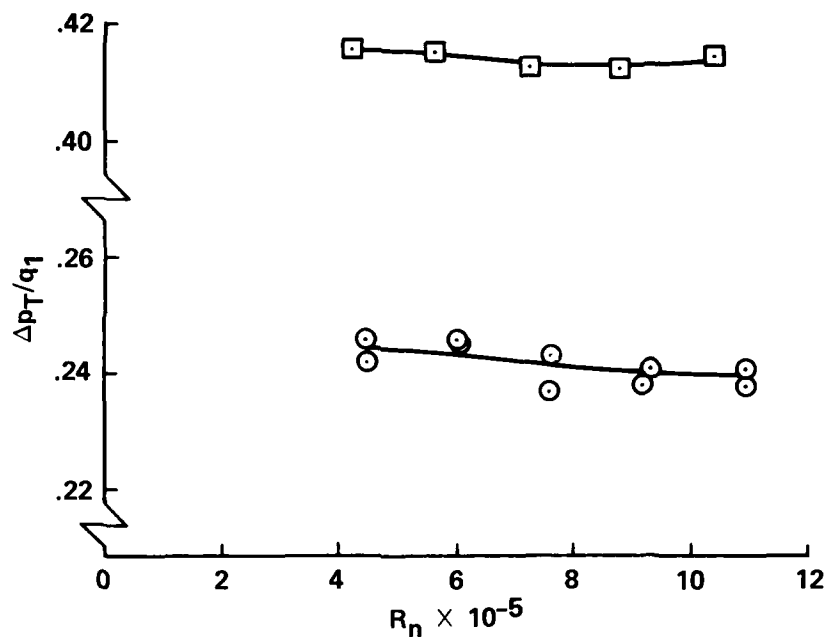
Figure 16.— 90° multiple-circular-arc turning vanes with movable tails.



CHORD-TO-GAP RATIO, c_v/g	BLOCKAGE, A_B/A_1 , %	COMPONENT AREA RATIO, A_2/A_1	HINGE GAP	FILLET ANGLE, θ_f , °
4.0	27.66	1.0	OPEN	NON.

(c) Pressure distributions for $\beta_{tot} = \beta_{net} = 90^\circ$, $\theta_f = 0^\circ$.

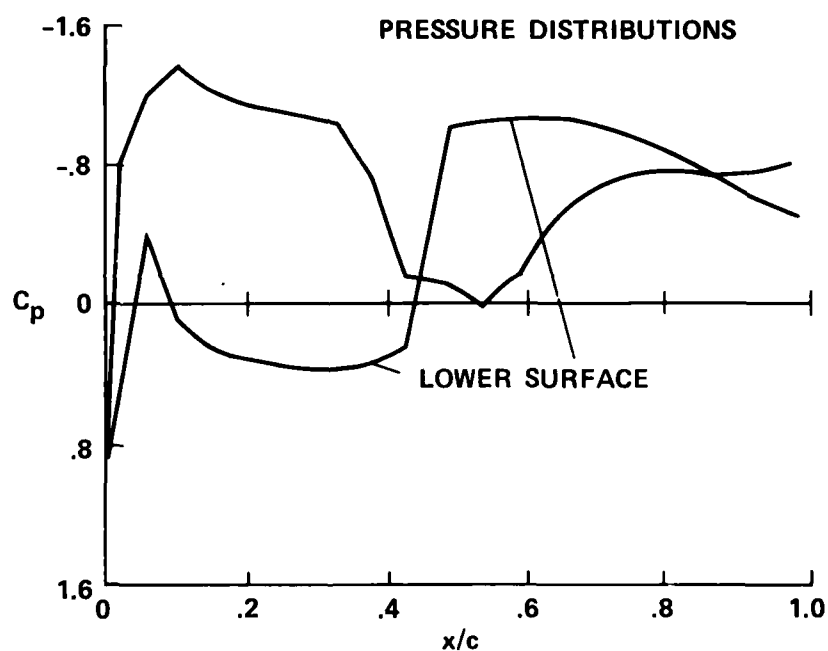
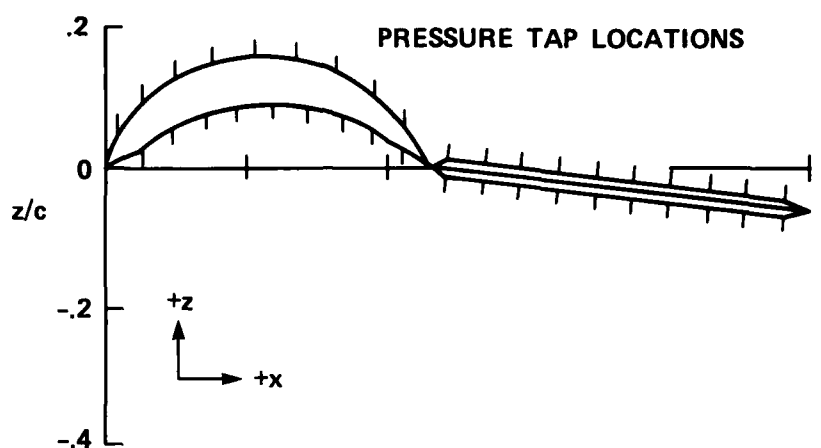
Figure 16.- Continued.



SYMBOL	CHORD-TO-GAP RATIO, c_v/g	BLOCKAGE $A_B/A_1, \%$	COMPONENT AREA RATIO, A_2/A_1	HINGE GAP	FILLET ANGLE, θ_f, deg	OVERTURN ANGLE, ϕ, deg
○	4.3	27.66	1.42	SEALED	NONE	0.6
□	↓	↓	↓	OPEN	↓	0.1

(d) Aerodynamic performance for $\beta_{\text{tot}} = 127.5^\circ$, $\beta_{\text{net}} = 52.5^\circ$, $\theta_t = 37.5^\circ$.

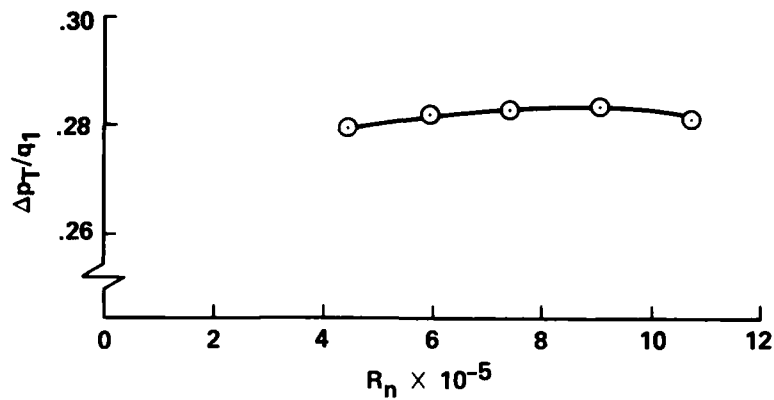
Figure 16.— Continued.



SYMBOL	CHORD-TO-GAP RATIO, c_v/g	BLOCKAGE A_B/A_1 , %	COMPONENT AREA RATIO, A_2/A_1	HINGE GAP	FILLET ANGLE, θ_f , deg
○	4.3	27.66	1.42	SEALED	NONE
□	↓	↓	↓	OPEN	↓

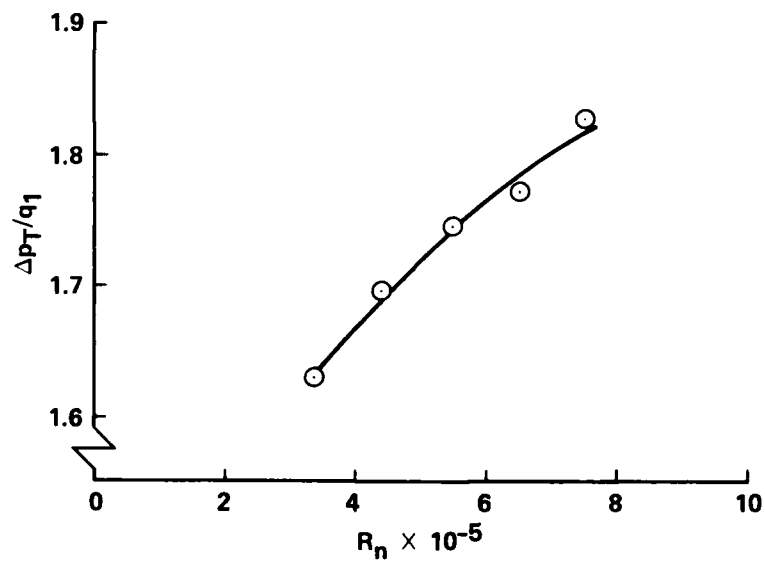
(e) Pressure distributions for $\beta_{tot} = 127.5^\circ$, $\beta_{net} = 52.5^\circ$, $\theta_i = 37.5^\circ$.

Figure 16.-- Continued.



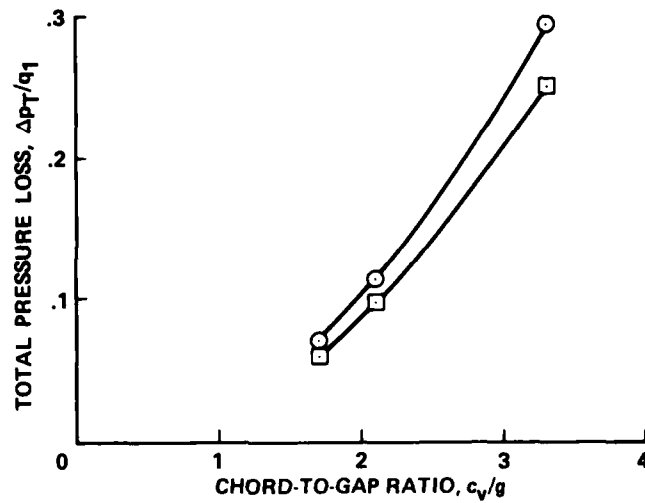
SYMBOL	CHORD-TO-GAP RATIO, c_v/g	BLOCKAGE A_B/A_1 , %	COMPONENT AREA RATIO, A_2/A_1	HINGE GAP	FILLET ANGLE, θ_f , deg	OVERTURN ANGLE, ϕ , deg
○	4.4	27.66	1.41	SEALED	NONE	-0.9

(f) Aerodynamic performance for $\beta_{tot} = 134.5^\circ$, $\beta_{net} = 45.5^\circ$, $\theta_f = 44.5^\circ$.



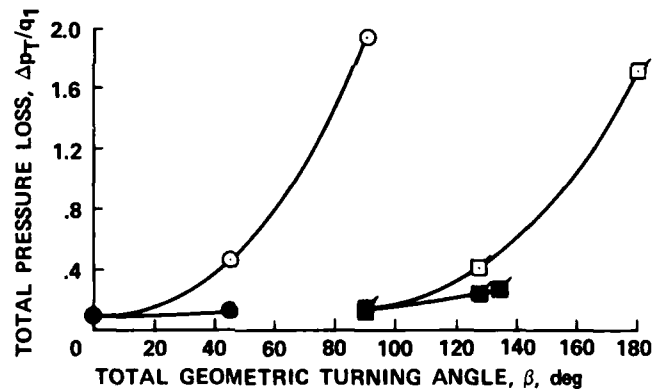
SYMBOL	CHORD-TO-GAP RATIO, c_v/g	BLOCKAGE, A_B/A_1 , %	COMPONENT AREA RATIO, A_2/A_1	HINGE GAP	FILLET ANGLE, θ_f , deg	OVERTURN ANGLE, ϕ , deg
○	4.0	27.66	1.22	OPEN	NONE	-8.0

(g) Aerodynamic performance for $\beta_{tot} = 180^\circ$, $\beta_{net} = 0^\circ$, $\theta_f = 90^\circ$.



SYMBOL	SURFACE GEOMETRY	REF. FIG.
○	FLAT	7
□	FAIRED	8

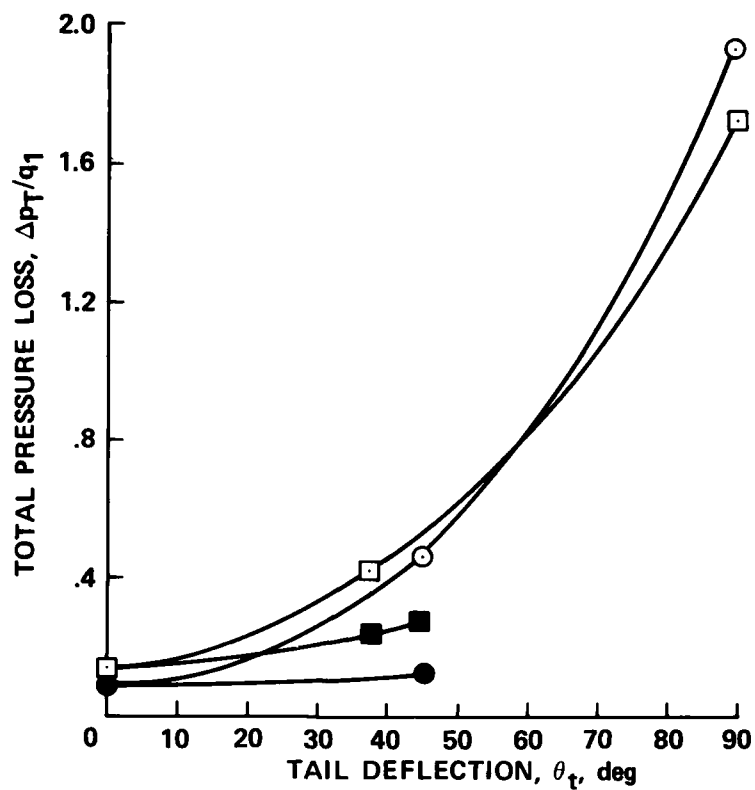
Figure 17.— Effect of vane spacing on pressure loss for flow straighteners with screen surface simulation at $R_H \approx 10^6$.



	VANE TYPE	REF. FIG.
○	THIN, $c_h/c = 0.5$ GAP OPEN	11 (i), (m)
●	GAP SEALED	11 (f), (i)
■	MULT.-CIRC.-ARC NO TAIL	15 (b)
□	TAIL GAP OPEN	16 (b), (d)
■	TAIL GAP SEALED	16 (d), (f), (g)

(a) Total turning angle.

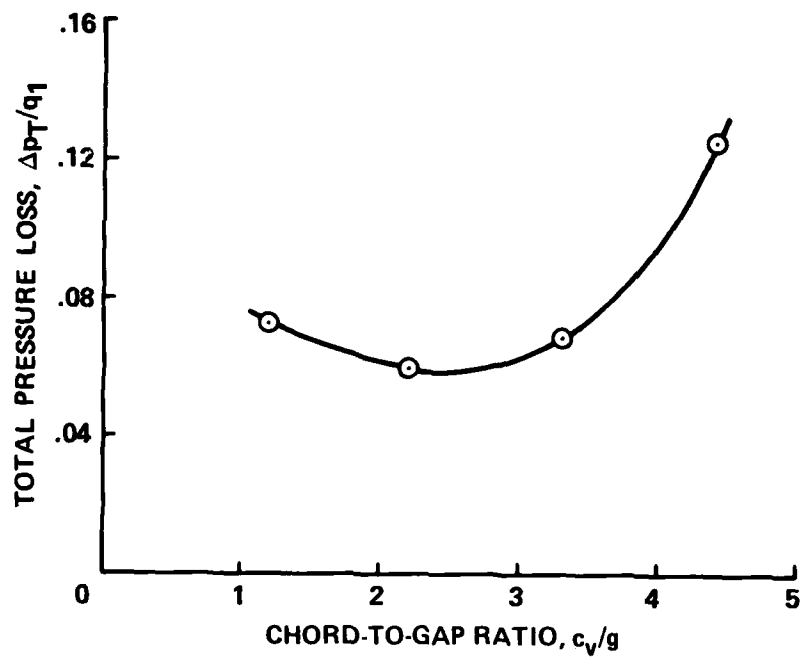
Figure 18.— Effect of turning angle on pressure loss for two types of vanes at $R_H \approx 5 \times 10^5$ and chord-to-gap ratio ≥ 4 .



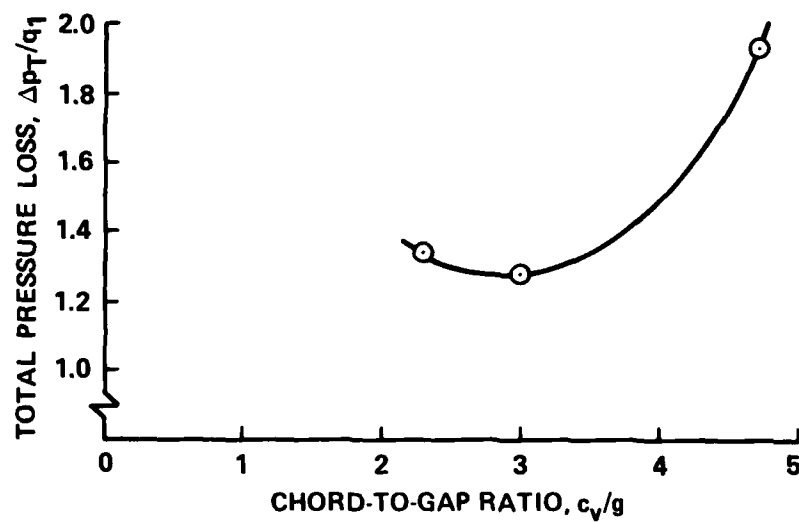
SYMBOL	VANE TYPE	REF. FIG.
○	THIN, $c_h/c = 0.5$ GAP OPEN	11 (i), (m)
●	GAP SEALED	11 (f), (i)
□	MULT.-CIRC.-ARC GAP OPEN	16 (b), (d)
■	GAP SEALED	16 (d), (f), (g)

(b) Tail deflection angle.

Figure 18.— Concluded.

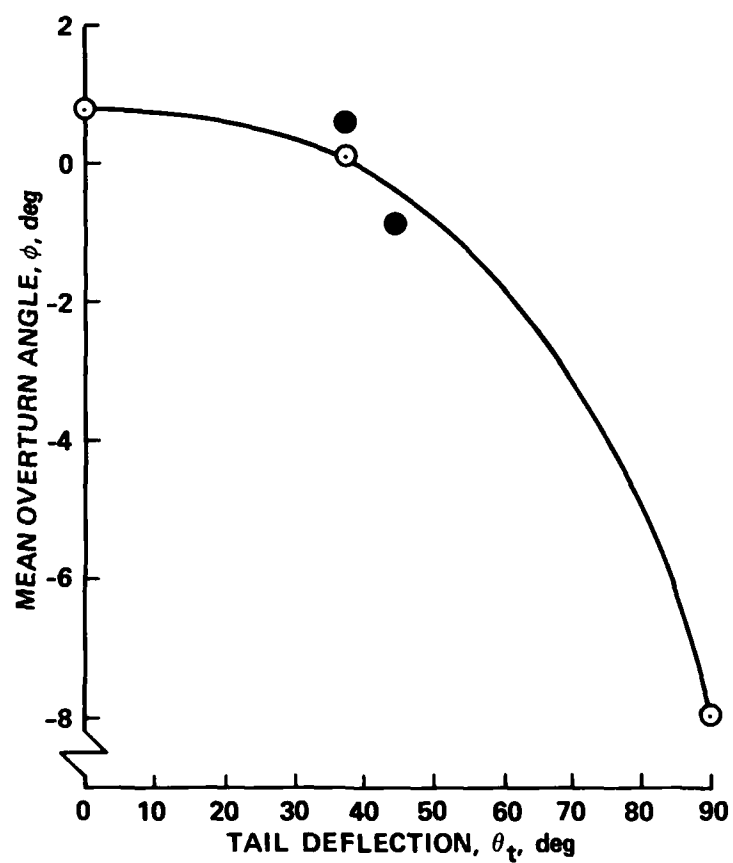


(a) Thin vanes (figs. 11(c) and 11(i)) at $\beta = 45^\circ$ with hinge-gap sealed.



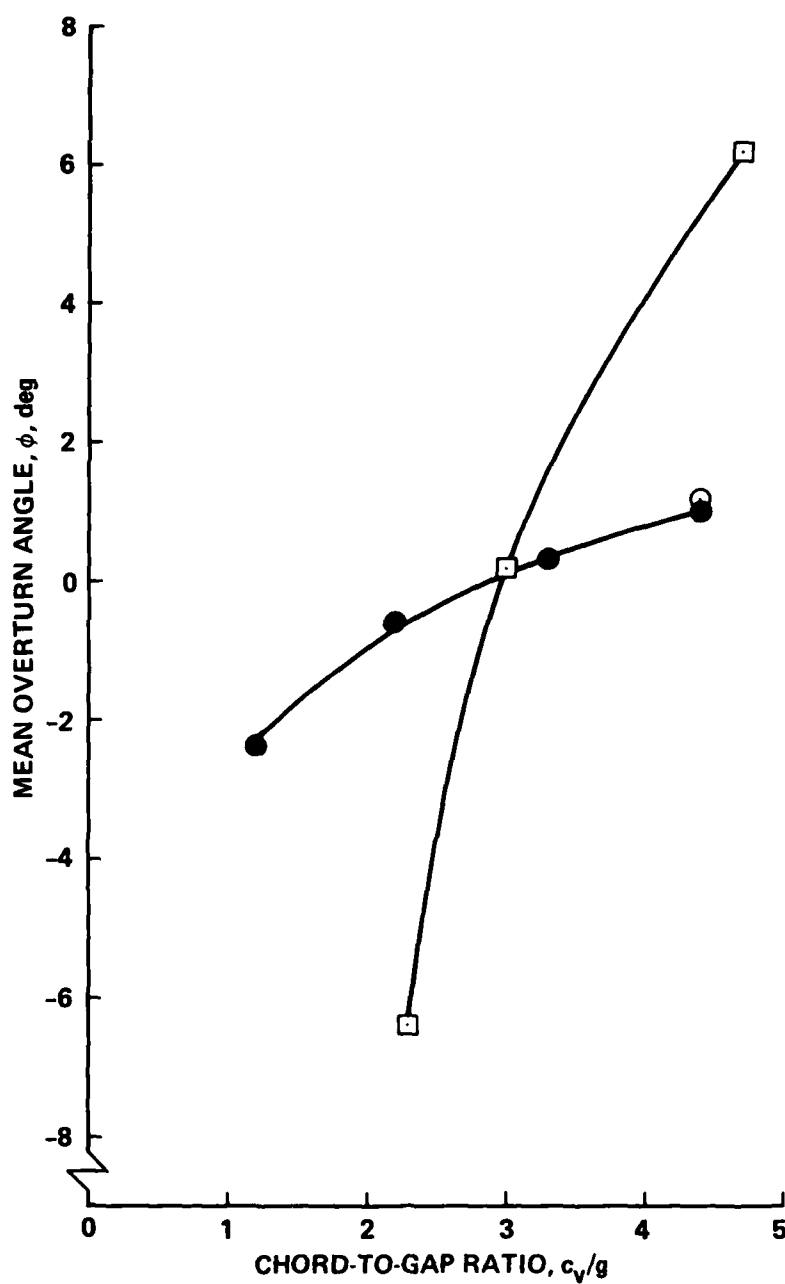
(b) Thin vanes (figs. 11(e) and 11(m)) at $\beta = 90^\circ$ with hinge gap open.

Figure 19.— Effect of chord-to-gap ratio on vane total-pressure loss.



	HINGE GAP	REF. FIG.
○	OPEN	16 (b), (d), (g)
●	SEALED	16 (d), (f)

Figure 20.— Flow overturn angle for multiple-circular-arc vanes with deflected tails.



TURNING ANGLE, deg	REF. FIG.
○ 45, GAP OPEN	11 (i)
● 45, GAP SEALED	11 (i)
□ 90, GAP OPEN	11 (m)

Figure 21.— Flow overturn angle for thin vanes at various spacings.

1. Report No. NASA TP-1972 AVRADCOM TR 82-A-2		2. Government Accession No. AD-A123952		3. Recipient's Catalog No.	
4. Title and Subtitle THE AERODYNAMIC PERFORMANCE OF SEVERAL FLOW CONTROL DEVICES FOR INTERNAL FLOW SYSTEMS				5. Report Date December 1982	
				6. Performing Organization Code	
7. Author(s) William T. Eckert,* Brian M. Wettlaufer,† and Kenneth W. Mort‡				8. Performing Organization Report No. A-8816	
9. Performing Organization Name and Address *AVRADCOM Research and Technology Laboratories, Ames Research Center, Moffett Field, Calif. 94035; †Sverdrup Technology, Ames Division, Moffett Field, Calif. 94035; ‡Ames Research Center, Moffett Field, Calif. 94035				10. Work Unit No. T-9391	
				11. Contract or Grant No.	
12. Sponsoring Agency Name and Address National Aeronautics and Space Administration, Washington, D.C. 20546 and U.S. Army Aviation Research and Development Command, St. Louis, MO 93166				13. Type of Report and Period Covered Technical Paper	
				14. Sponsoring Agency Code 505-42-81-00-00	
15. Supplementary Notes Point of contact: Bill Eckert, Ames Research Center, Mail Stop 215-2, Moffett Field, Calif. 94035 (415) 965-6087 or FTS 448-6087					
16. Abstract An experimental research and development program was undertaken to develop and document new flow-control devices for use in the major modifications to the 40- by 80-Foot Wind Tunnel at Ames Research Center. These devices, which are applicable to other facilities as well, included grid-type and quasi-two-dimensional flow straighteners, louver panels for valving, and turning-vane cascades with net turning angles from 0 ^{deg} to 90 ^{deg} . The tests were conducted at model scale over a Reynolds number range from 2X10 ⁵ to 17X10 ⁵ , based on chord. The results showed quantitatively the performance benefits of faired, low-blockage, smooth-surface straightener systems, and the advantages of curved turning-vanes with hinge-line gaps sealed and a preferred chord-to-gap ratio between 2.5 and 3.0 for 45 ^{deg} or 90 ^{deg} turns.					
17. Key Words (Suggested by Author(s)) Wind tunnels, Cascades, Grids, Duct losses, Ducts, Throttles, Pressure losses, Flow control, Valves, Efficiency, Vanes, Flow straighteners, Louvers, Baffles				18. Distribution Statement Unclassified - Unlimited Subject Category 09	
19. Security Classif. (of this report) Unclassified		20. Security Classif. (of this page) Unclassified		21. No. of Pages 48	
				22. Price* AO3	

*For sale by the National Technical Information Service, Springfield, Virginia 22161

